Beijing Climate Center Earth System Model version 1 (BCC-ESM1): Model Description and Evaluation of Aerosol Simulations

Tongwen Wu[1*], Fang Zhang[1], Jie Zhang[1], Weihua Jie[1], Yanwu Zhang[1], Fanghua Wu[1], Laurent Li[1,2], Jinghui Yan[1], Xiaohong Liu[3], Xiao Lu[4], Haiyue Tan[4], Lin Zhang[4], Jun Wang[5], Aixue Hu[6]

[1]Beijing Climate Center, China Meteorological Administration, Beijing, China

[2]Laboratoire de Météorologie Dynamique, IPSL, CNRS, Sorbonne Université, Ecole Normale Supérieure, Ecole Polytechnique, Paris, France

[3] Texas A&M University, College Station, TX, USA

[4] Laboratory for Climate and Ocean-Atmosphere Studies, Department of Atmospheric and Oceanic Sciences, School of Physics, Peking University, Beijing, China

[5] University of Iowa, Iowa City, IA 52242, USA

[6]National Center for Atmospheric Research, PO Box 3000, Boulder, Colorado 80307-3000, USA

Correspondence to: Tongwen Wu (twwu@cma.gov.cn)

Submit to Geosci. Model Dev.

Revised on Oct. 23, 2019

Abstract. BCC-ESM1 is the first version of a fully-coupled Earth System Model with interactive atmospheric chemistry and aerosols developed by the Beijing Climate Center, China Meteorological Administration. Major aerosol species (including sulfate, organic carbon, black carbon, dust and sea salt) and greenhouse gases are interactively simulated with a whole panoply of processes controlling emission, transport, gas-phase chemical reactions, secondary aerosol formation, gravitational settling, dry deposition, and wet scavenging by clouds and precipitation. Effects of aerosols on radiation, cloud, and precipitation are fully treated. The performance of BCC-ESM1 in simulating aerosols and their optical properties is comprehensively evaluated as required by the Aerosol Chemistry Model Intercomparison Project (AerChemMIP), covering the preindustrial mean state and time evolution from 1850 to 2014. The simulated aerosols from BCC-ESM1 are quite coherent with CMIP5-recommended data, in-situ measurements from surface networks (such as IMPROVE in the U.S. and EMEP in Europe), and aircraft observations. A comparison of modeled aerosol optical depth (AOD) at 550 nm with satellite observations retrieved from Moderate Resolution Imaging Spectroradiometer (MODIS) and Multi-angle Imaging SpectroRadiometer (MISR) and surface AOD observations from AErosol RObotic NETwork (AERONET) shows reasonable agreements between simulated and observed AOD. However, BCC-ESM1 shows weaker upward transport of aerosols from the surface to the middle and upper troposphere, likely reflecting the deficiency of representing deep convective transport of chemical species in BCC-ESM1. With an overall good agreement between BCC-ESM1 simulated and observed aerosol properties, it demonstrates a success of the implementation of interactive aerosol and atmospheric chemistry in BCC-ESM1.

1. Introduction

Atmosphere is a thin gaseous layer around the Earth, consisting of nitrogen, oxygen and a large number of trace gases including important greenhouse gases (GHG) such as water vapor, tropospheric ozone (O_3), carbon dioxide (CO_2), methane (CH_4), nitrous oxide (N_2O), and chloro-fluoro-carbons (CFCs). Besides gaseous components, atmosphere also contains various aerosols, which are important for cloud formation and radiative transfer. Atmospheric trace gases and aerosols are actually interactive components of the climate system. Their inclusion in global climate models (GCMs) is a significant enhancement for most state-of-the-art climate models (Lamarque et al., 2013; Collins et al., 2017). Early attempts in coupling global climate dynamics with atmospheric chemistry can be traced back to late 1970s, when 3D transport of ozone and simple stratospheric chemistry were firstly incorporated into a GCM to simulate global O_3 production and transport (e.g., Cunnold et al. 1975; Schlesinger and Mintz 1979). Since mid-1980s, a large number of on-line global climate/chemistry models have been developed to address issues of the Antarctic stratospheric O_3 depletion (e.g., Cariolle et al. 1990; Austin et al. 1992; Solomon, 1999), tropospheric O_3 and sulfur cycle (e.g., Feichter et al. 1996; Barth et al. 2000), tropospheric aerosol and its interactions with cloud (e.g., Chuang et al. 1997; Lohmann et al. 2000; Ghan and Easter, 2006; Jacobson 2012). Aerosols and chemically reactive gases in the atmosphere exert important influences on global and regional air quality and climate (Collins et al., 2017).

Since 2013, the Beijing Climate Center (BCC), China Meteorological Administration, has continuously developed and updated its fully-coupled GCM, the Beijing Climate Center Climate System Model (BCC-CSM) (Wu et al., 2013; Wu et al., 2014; Wu et al., 2019). BCC-CSM version 1.1 was one of the comprehensive carbon-climate models participating in the phase five of the Coupled Model Intercomparison Project (CMIP5, Taylor et al. 2012). When forced by prescribed historical emissions of CO_2 from combustion of fossil fuels and land use change, BCC-CSM1.1 successfully reproduced the trends of observed atmospheric CO_2 concentration and global surface air temperature from 1850 to 2005 (Wu et al., 2013). During recent years, BCC-CSM1.1 has been used in numerous investigations on soil organic carbon changes (e.g. Todd-Brown et al., 2014), ocean biogeochemistry changes (e.g. Mora et al., 2013), and carbon-climate feedbacks (e.g. Arora et al., 2013; Hoffman et al., 2014).

BCC-CSM includes main climate-carbon cycle processes (Wu et al., 2013) and the global mean atmospheric CO_2 concentration is calculated from a prognostic equation of CO_2 budget taking into account global anthropogenic CO_2 emissions and interactive land-atmosphere and ocean-atmosphere CO2 exchanges.

In recent years, BCC has put large efforts in developing a global climate-chemistry-aerosol fully-coupled Earth System Model (BCC-ESM1) on the basis of BCC-CSM2 (Wu et al., 2019). The objective is to interactively simulate global aerosols (e.g. sulfate, black carbon, etc.) and main greenhouse gases (e.g. O_3, CH_4, NO_2 and CO_2) in the atmosphere and to investigate feedbacks between climate and atmospheric chemistry. BCC-ESM1 is at the point to be publicly released, and it is actively used by BCC for several CMIP6-endorsed research initiatives (Eyring et al. 2016), including the Aerosol Chemistry Model Intercomparison Project (AerChemMIP, Collins et al., 2017) and the Coupled Climate–Carbon Cycle Model Intercomparison Project (C4MIP, Jones et al. 2016).

The purpose of this paper is to evaluate the performance of BCC-ESM1 in simulating aerosols and their optical properties in the 20th century. The description of BCC-ESM1 is presented in Section 2. The experimental protocol is given in Section 3. Section 4 presents the evaluations of aerosol simulations with comparisons to CMIP5-recommended data (Lamarque et al., 2010) and data obtained from both global surface networks and satellite observations. The regional and global characteristics compared to observations and estimates from other studies are analyzed. Simulations of aerosol optical properties in the 20th century are also analyzed in Section 4. Conclusions and discussions are summarized in Section 5. Information about code and data availability is given in Section 6.

2. Model description

BCC-ESM1 is an Earth System Model with interactive chemistry and aerosol components, in which the atmospheric component is BCC Atmospheric General Model version 3 (Wu et al., 2019) with interactive atmospheric chemistry (hereafter BCC-AGCM3-Chem), land component BCC Atmosphere and Vegetation Interaction Model version 2.0 (hereafter BCC-AVIM2.0), ocean component Modular Ocean Model version 4 (MOM4)-L40, and sea ice component [sea ice simulator (SIS)]. Different components of BCC-ESM1 are fully coupled and interact with each other through fluxes of momentum,

energy, water, carbon and other tracers at their interfaces. The coupling between the atmosphere and the ocean is done every hour.

The atmospheric component BCC-AGCM3-Chem is able to simulate global atmospheric composition and aerosols from anthropogenic emissions as forcing agents. Its resolution is T42 (approximately 2.8125ºx2.8125º transformed spectral grid). The model has 26 levels in a hybrid sigma/pressure vertical coordinate system with the top level at 2.914 hPa. Details of the model physics are described in Wu et al. (2019). The BCC-AGCM3-Chem combines 66 gas-phase chemical species and 13 bulk aerosol compounds as listed in Table 1. Apart from 3 gas-phase species of dimethyl sulfide (DMS), SO_2 and NH3, the other 63 gas-phase species are the same as those in the "standard version" of MOZART2 (Model for Ozone and Related chemical Tracers, version 2), a global chemical transport model for the troposphere developed by the National Center for Atmospheric Research (NCAR) driven by meteorological fields from either climate models or assimilations of meteorological observations (Horowitz et al., 2003). Advection of all tracers in BCC-AGCM3-Chem is performed through a semi-Lagrangian scheme (Williamson and Rasch, 1989), and vertical diffusion within the boundary layer follows the parameterization of Holtslag and Boville (1993). The gas-phase chemistry of the 63 MOZART2 gas-phase species as listed in Table 1 is treated in the same way as that in the "standard version" of MOZART2 (Horowitz et al., 2003), and there are 33 photolytic reactions and 135 chemical reactions involving 30 dry deposited chemical species and 25 soluble gas-phase species. Dry deposition velocities for the 15 trace gases including O_3, CO, CH_4, CH_2O, CH_3OOH, H_2O_2, NO_2, HNO_3, PAN, CH_3COCH_3, CH_3COOOH, CH_3CHO, CH_3COCHO, NO, and HNO_4 are not computed interactively and directly interpolated from MOZART2 climatological monthly mean deposition velocities (https://en.wikipedia.org/wiki/MOZART(model)) which are calculated offline (Bey et al., 2001; Shindell et al., 2008) using a resistance-in-series scheme originally described in Wesely (1989). The dry deposition velocities for the other 15 species including MPAN, ONIT, ONITR, C_2H_5OH, POOH, C_2H_5OOH, C_3H_7OOH, ROOH, GLYALD, HYAC, CH_3OH, MACROOH, ISOPOOH, XOOH, HYDRALD, and H_2 are calculated using prescribed deposition velocities of O_3, CO, CH_3CHO, or land surface type and surface temperature following the MOZART2 (Horowitz et al., 2003). Wet removals by in-cloud scavenging for 25 soluble gas-phase species

in the “standard version” of MOZART2 use the parameterization of Giorgi and Chameides (1985) based on their temperature dependent effective Henry’s law constants. In-cloud scavenging is proportional to the amount of cloud condensate converted to precipitation, and the loss rate depends on the amount of cloud water, the rate of precipitation formation, and the rate of tracer uptake by the liquid phase water. Other highly soluble species such as HNO_3, H_2O_2, ONIT, ISOPOOH, MACROOH, XOOH, and Pb-210 are also removed by below-cloud washout as calculated using the formulation of Brasseur et al. (1998). Below-cloud scavenging is proportional to the precipitation flux in each model layer and the loss rate depends on the precipitation rate. Vertical transport of gas tracers and aerosols due to deep convection is not yet included in the present version of BCC-AGCM3-Chem, which process is considered as a part of the deep convection and occurs generally in a small spatial region on a GCM-box with low-resolution (2.8°lat.×2.8°lon.). Another consideration is that a large uncertainty exists to treat transport of those water-soluble tracers by deep convection. But this effect will be involved in the next version of BCC model.

The BCC-AVIM2.0 is the land model with terrestrial carbon cycle. It is described in details in Li et al. (2019) and includes biophysical, physiological, and soil carbon-nitrogen dynamical processes. The terrestrial carbon cycle operates through a series of biochemical and physiological processes on photosynthesis and respiration of vegetation. Biogenic emissions from vegetation are computed online in BCC-AVIM2.0 following the algorithm of the Model of Emissions of Gases and Aerosols from Nature version 2.1 (MEGAN2.1, Guenther et al., 2012).

The oceanic component of BCC-ESM1 is the Modular Ocean Model version 4 with 40 levels (hereafter MOM4-L40), and the sea ice component Sea Ice Simulator (SIS). MOM4-L40 uses a tripolar grid of horizontal resolution with 1º longitude by 1/3º latitude between 30ºS and 30ºN ranged to 1º longitude by 1º latitude from 60ºS and 60ºN poleward and 40 z-levels in the vertical. Carbon exchange between the atmosphere and the ocean are calculated online in MOM4-L40 using a biogeochemistry module that is based on the protocols from the Ocean Carbon Cycle Model Intercomparison Project–Phase 2 (OCMIP2, http://www.ipsl.jussieu.fr/OCMIP/phase2/). SIS has the same horizontal resolution as MOM4-L40 and three layers in the vertical, including one layer of snow cover and two layers

of equally sized sea ice. Details of oceanic component MOM4-L40 and sea-ice component SIS that are used in BCC-ESM1 may be found in Wu et al. (2013) and Wu et al. (2019).

In the following sub-sections, we will describe the treatments in BCC-ESM1 for 3 gas-phase species of DMS, SO_2 and NH_3, 13 prognostic aerosol species including sulfate (SO_4^{2-}), 2 types of organic carbon (hydrophobic OC1, hydrophilic OC2), 2 types of black carbon (hydrophobic BC1, hydrophilic BC2), 4 categories of soil dust (DST01, DST02, DST03, DST04), and 4 categories of sea salt (SSLT01, SSLT02, SSLT03, SSLT04). Concentrations of all aerosols in BCC-ESM1 are mainly determined by advective transport, emission, dry deposition, gravitational settling, and wet scavenging by clouds and precipitation, except for SO_4^{2-} which gas-phase and aqueous phase conversion from SO_2 are also considered. The present version of aerosol scheme belongs to a bulk aerosol model and mainly refers to the scheme of CAM-Chem (Lamarque et al., 2012), but the nucleation and coagulation of aerosols are still ignored.

2.1 SO_2, DMS, NH_3, and Sulfate

SO_2 is a main sulfuric acid precursor to form aerosol sulfate SO_4^{2-}. Conversions of SO_2 to SO_4^{2-} occur by gas phase reactions (Table 2) and by aqueous phase reactions in cloud droplets. The dry deposition velocity of SO_2 follows the resistance-in-series approach of Wesely (1989) using the formula, $W_{SO2} = 1/(r_a + r_b + r_c)$, in which r_a, r_b, *and* r_c are the aerodynamic resistance, the quasi-laminar boundary layer resistance, and the surface resistance, respectively and they are interactively computed in each model time step. The loss rate of SO_2 due to wet deposition is computed following the scheme in the global Community Atmosphere Model (CAM) version 4, the atmospheric component of the Community Earth System Model (Lamarque et al., 2012).

The sources of SO_2 mainly come from fuel combustion, industrial activities, and volcanoes. SO_2 can also be formed from the oxidation of DMS as listed in Table 2 in which their reaction rates follow CAM-Chem (Lamarque et al. 2012). The main source of DMS is from oceanic emissions via biogenic processes. It is prescribed with the climatological monthly data that are extracted from MOZART2 package (https://www2.acom.ucar.edu/gcm/mozart-4). SO_4^{2-} is one of the prognostic aerosols in BCC-AGCM3-Chem. Its treatment follows CAM4-Chem (Lamarque et al., 2012). It is

produced primarily by the gas-phase oxidation of SO_2 (in Table 2) and by aqueous phase oxidation of SO_2 in cloud droplets. The gas phase reactions, rate constants, and gas-aqueous equilibrium constants are given by Tie et al. (2001). The heterogeneous reactions of SO_4^{2-} occur on all aerosol surfaces. Their treatment follows a Bulk Aerosol Model (BAM) used in CAM4 (Neale et al., 2010). The heterogeneous reactions depend strongly on pH values in clouds which are calculated from the concentrations of SO_2, HNO_3, H_2O_2, NH_3, O_3, HO_2, and SO_4^{2-}. NH_3 is a gas tracer apart from MOZART2 (Table 1). Its sources include aircraft and surface emissions due to anthropogenic activity, biomass burning, and biogenic emissions from land soil and ocean surfaces (Table 4). SO_4^{2-} is assumed to be all in aqueous phase due to water uptake, although Wang et al. (2008a) showed that ~34% of sulfate particles are in solid phase globally due to the hysteresis effect of ammonium sulfate phase transition. However, in terms of radiative forcing, consideration of solid sulfate formation process lowers the sulfate forcing by ~8% as compared to consideration of all sulfate particles in aqueous phase (Wang et al., 2008b). Future model development may consider the life cycle of NH_3. The sulfate in- and below-cloud scavenging follows Neu and Prather (2011). Washout of SO_4^{2-} is set to 20% of the washout rate of HNO_3 following Tie et al. (2005) and Horowitz (2006). Dry deposition velocity of SO_4^{2-} is also calculated by the resistance-in-series approach.

2.2 Aerosols of organic carbon and black carbon

BCC-AGCM3-Chem treats two types of organic carbon (OC), i.e. water-insoluble tracer OC1 and water-soluble tracer OC2, and two types of black carbon (BC), i.e. water-insoluble tracer BC1 and water-soluble tracer BC2. As shown in Table 2, hydrophobic BC1 and OC1 can be converted to hydrophilic BC2 and OC2 with a constant rate of 7.1×10^{-6} s^{-1} (Cooke and Wilson, 1996). The 4 tracers of organic carbon and black carbon are mainly from emissions including both fossil fuel and biomass burning, and are from the CMIP6 data package (https://esgf-node.llnl.gov/search/input4mips/, Hoesly et al., 2018). Beside anthropogenic and biomass burning emissions, hydrophilic organic carbon OC2 can also come from natural biogenic volatile organic compound (VOC) emissions. Dry deposition velocities for all the 4 OC and BC tracers are set to $0.001 m.s^{-1}$. OC2 and BC2 are soluble aerosols, and their sinks are primarily governed by wet deposition. Their in- and below-cloud scavenging follows the

scheme of Neu and Prather (2011).

2.3 Sea salt aerosols

As shown in Table 3, sea salt aerosols in the model are classified into four size bins (0.2–1.0, 1.0–3.0, 3.0–10, and 10–20 μm) in diameter. They originate from oceans and are calculated online by BCC-ESM1. The upward flux $F_{sea-salt}$ of sea salt productions for four bins is proportional to the 3.41 power of the wind speed u_{10m} at 10 m height near the sea surface (Mahowald et al., 2006) and is expressed as

$$F_{sea-salt} = S \cdot (u_{10m})^{3.41}, \quad (1)$$

where S is a scaling factor and set to $4.05\text{x}10^{-15}$, $4.52\text{x}10^{-14}$, $1.15\text{x}10^{-13}$, $1.20\text{x}10^{-13}$ for four size bins of sea salt aerosols in BCC-ESM1, respectively.

Dry deposition of sea salts depends on the turbulent deposition velocity in the lowest atmospheric layer using aerodynamic resistance and the friction velocity, and the settling velocity through the whole atmospheric column for each bin of sea salts. The turbulent deposition velocity and settling velocity depend on particle diameter and density (listed in Table 3). In addition, the fact that the size of sea salts changes with humidity is also considered. The wet deposition of sea salts follows the scheme for soluble aerosols used in CAM4, and depends on prescribed solubility and size-independent scavenging coefficients.

2.4 Dust aerosols

Dust aerosols behave in a similar way as sea salts. Their variations involve three major processes: emission, advective transport, and wet/dry depositions. The dust emission is based on a saltation-sandblasting process, and depends on wind friction velocity, soil moisture, and vegetation/snow cover (Zender et al., 2003). The vertical flux of dust emission is corrected by a surface erodible factor at each model grid cell which has been downloaded from NCAR website (https://svn-ccsm-inputdata.cgd.ucar.edu/trunk/inputdata/atm/cam/dst/). Soil erodibility is prescribed by a physically-based geomorphic index that is proportional to the runoff area upstream of each source region (Albani et al., 2014). Like sea salts, dry deposition of dust aerosols includes gravitational and turbulent deposition processes, while wet deposition results from both convective and large scale precipitation and is dependent on prescribed size-independent scavenging coefficients.

2.5 Effects of aerosols on radiation, clouds, and precipitation

The mass mixing ratios of bulk aerosols are prognostic variables in BCC-ESM1 and directly affect the radiative transfer in the atmosphere with their treatments following the NCAR Community Atmosphere Model (CAM3, Collins et al., 2004). Indirect effects of aerosols are taken into account in the present version of BCC-AGCM3-Chem (Wu et al., 2019). Aerosol particles act as cloud condensation nuclei and exert influence on cloud properties and precipitation, and ultimately impact the hydrological cycle.

Prognostic aerosol masses are used to estimate the liquid cloud droplet number concentration N_{cdnc} (cm^{-3}) in BCC-AGCM3-Chem. N_{cdnc} is explicitly calculated using the empirical function suggested by Boucher and Lohmann (1995) and Quaas et al. (2006):

$$N_{cdnc} = \exp\left[5.1 + 0.41\ln\left(m_{aero}\right)\right] \tag{2}$$

where m_{aero} ($\mu\ \mathrm{g.m}^{-3}$) is the total mass of all hydrophilic aerosols,

$$m_{aero} = m_{SS} + m_{OC} + m_{SO_4} + m_{NH_4NO_2}\ , \tag{3}$$

i.e. the first bin of sea salt ($\mathrm{m_{SS}}$), hydrophilic organic carbon (m_{OC}), sulphate (m_{SO_4}), and NH_4NO_2. A dataset of NH_4NO_2 from NCAR CAM-Chem (Lamarque et al., 2012) is used in our model.

N_{cdnc} is an important factor in determining the effective radius of cloud droplets for radiative calculation. The effective radius of cloud droplets r_{el} is estimated as

$$r_{el} = \beta \cdot r_{l,vol}\ , \tag{4}$$

where β is a parameter dependent on the droplets spectral shape and follows the calculation proposed by Peng and Lohmann (2003),

$$\beta = 0.00084 N_{cdnc} + 1.22\ . \tag{5}$$

$r_{l,vol}$ is the volume-weighted mean cloud droplet radius,

$$r_{l,vol} = \left[\left(3LWC\right)/\left(4\pi\rho_w N_{cdnc}\right)\right]^{1/3}, \tag{6}$$

where ρ_{w} is the liquid water density and LWC the cloud liquid water content ($\mathrm{g\ cm}^{-3}$).

Aerosols also exert impacts on precipitation efficiency (Albrecht, 1989), which is taken into account in the parameterization of non-convective cloud processes. There are five processes that convert condensate to precipitate: auto-conversion of liquid water to rain, collection of cloud water by rain, auto-conversion of ice to snow, collection of ice by snow,

and collection of liquid by snow. The auto-conversion of cloud liquid water to rain (*PWAUT*) is dependent on the cloud droplet number concentration and follows a formula that was originally suggested by Chen and Cotton (1987),

$$PWAUT = C_{l,aut}\hat{q}_l^2\rho_a / \rho_w \left(\frac{\hat{q}_l \rho_a}{\rho_w N_{ncdc}} \right)^{1/3} H\left(r_{l,vol} - r_{lc,vol}\right) \quad (7)$$

Where $\hat{q}_l$ is in-cloud liquid water mixing ratio, ρ_a and ρ_w are the local densities of air and water respectively, and $C_{l,aut}$ is a constant. $H(x)$ is the Heaviside step function with the definition,

$$H\left(x\right) = \begin{cases} 0, & x < 0 \\ 1, & x \geq 0 \end{cases}. \quad (8)$$

$r_{lc,vol}$ is the critical value of mean volume radius of liquid cloud droplets $r_{l,vol}$, and set to 15 μ m.

3. Experiment design for the 20th century climate simulation

There is an Aerosol Chemistry Model Intercomparison Project (AerChemMIP, Collins et al., 2017) endorsed by the Coupled-Model Intercomparison Project 6 (CMIP6) for documenting and understanding past and future changes in the chemical composition of the atmosphere, and estimating the global-to-regional climate response from these changes. Modelling groups with full chemistry and aerosol models are encouraged to perform all AerChemMIP simulations (Collins et al., 2017). To assess the ability of our model to simulate aerosols (mean and variability), we have followed the historical simulation designed by CMIP6 (Eyring et al., 2016) which is named as "historical" experiment in the Earth System Grid Federation (ESGF). The protocol details of the historical experiment forced with emissions evolving from 1850 to 2014 refer to Collins et al. (2017). O_3 in the historical simulation is an interactive prognostic variable and feedbacks on radiation, and the concentrations of other WMGHG, e.g. CH_4, N_2O, CO_2, CFC11, and CFC12 are prescribed using CMIP6 historical forcing data as suggestion in AerChemMIP protocol. Although CH_4 and N_2O are prognostic variables in the chemistry scheme (Table 1), their prognostic values at each model step in the historical experiment are replaced by CMIP6 data. The rest of historical forcing data include: (1) yearly global gridded land-use forcing data sets, and (2)

315 solar forcing. All these datasets were downloaded from
316 https://esgf-node.llnl.gov/search/input4mips/. Climate feedback processes that involve changes
317 to the atmospheric composition of reactive gases and aerosols may affect the temperature
318 response to a given WMGHG concentration level (Collins et al., 2017). Three members of
319 historical experiments are conducted and the first member is analyzed in this work.

320 **3.1 Surface emissions**

321 Surface emissions of chemical species from different sources are summarized in Table
322 4. They include anthropogenic emissions from fossil fuel burning and other industrial
323 activities, biomass burning (including vegetation fires, fuel wood and agricultural burning),
324 biogenic emissions from vegetation and soils, and oceanic emissions. Most historical
325 emissions from anthropogenic source (surface, aircraft plus ship) and biomass burning from
326 1850 to 2014 are CMIP6-recommended data (Hoesly et al., 2018; available at
327 https://esgf-node.llnl.gov/search/input4mips). Anthropogenic or biomass burning sources of
328 some tracers which are not included in the CMIP6 dataset (see Table 4), anthropogenic
329 emission of H_2 and N_2O are from monthly climatological dataset provided by the MOZART-2
330 standard package. N_2O is a prognostic variable in BCC-ESM1 but it is replaced by CMIP6
331 prescribed concentration in the historical run. Other emissions including biomass burning
332 (CH_3COCH_3) and anthropogenic emission (CH_3CHO, CH_3OH, and CH_3COCH_3) are from the
333 IPCC ACCMIP emission inventory (http://accent.aero.jussieu.fr/ACCMIP.php) covering the
334 period from 1850 to 2010 with 10-year intervals (see Table 4). Monthly lumped emissions of
335 black carbon and organic carbon aerosols from 1850 to 2014 are downloaded from
336 CMIP6-recommended data, but we used 80% (for BC) and 50% (for OC) of them in their
337 hydrophobic forms (BC1 and OC1) and the rest in their hydrophilic forms (BC2 and OC2),
338 following the work of Chin et al. (2002).

339 Five tracers of ISOP, ACET (CH_3COCH_3), C_2H_4, C_3H_8, and Monoterpenes ($C_{10}H_{16}$) in
340 Table 1 belong to biogenic volatile organic carbons (VOCs). As shown in Table 4, those
341 VOCs emissions are online calculated in BCC-ESM1 following the modeling framework of
342 the Model of Emissions of Gases and Aerosols from Nature version 2.1 (MEGAN2.1,
343 Guenther et al., 2012) using simple mechanistic algorithms to account for major known
344 processes controlling biogenic emissions. The MEGAN2.1 can provide a flexible scheme for

estimating 16 tracers of biogenic emissions from terrestrial ecosystems including five VOCs emissions used in BCC-ESM1 (Table 4). All the VOCs emissions depend on current and past surface air temperature, solar flux, and the landscape types. Their calculation requires global maps of plant functional type (PFT) and leaf area index (LAI) which is a prognostic variable from the land model BCC-AVIM2. The effect of atmospheric CO_2 concentration on isoprene emissions is included. 10% of the biogenic monoterpenes emissions as calculated online with the MEGAN2.1 algorithm in BCC-AVIM2 are converted to hydrophilic organic carbon (OC2) to account for formation of secondary organic aerosols following Chin et al. (2002) in this version of BCC-ESM1.

3.2 Volcanic eruption, lightning and aircraft emissions

As there is no stratospheric aerosol scheme in BCC-ESM1, concentrations of sulfate aerosol at heights from 5 to 39.5 km, which volcanic origin, are directly prescribed using the CMIP6-recommended data (Thomasson et al., 2018) from 1850 to 2014. The effects of surface SO_2 emissions from volcanic eruption on the variation of SO2 in the atmosphere and then on the variation of tropospheric SO_4^{2-} concentration are considered, and the SO_2 emissions from 1850 to 2014 are downloaded from the IPCC ACCMIP emission inventory (http://accent.aero.jussieu.fr/ACCMIP.php). Aircraft emissions are provided for NO_2, CO, CH_4, NH_3, NO, SO_2, and aerosols of OC and BC (Table 1). The emissions of NO from lightning are online calculated in BCC-AGCM3-Chem following the parameterization in MOZART2, and the globally-averaged mean during the period of 1850 to 2014 is 5.19 $Tg(N)\cdot yr^{-1}$, which is in agreement with observations within the range of 3 to 6 $Tg(N)\cdot yr^{-1}$ (Martin et al., 2002). The lightning frequency depends strongly on the convective cloud top height, and the ratio of cloud-to-cloud versus cloud-to-ground lightning depends on the cold cloud thickness from the level of 0℃ to the cloud top (Price and Rind, 1992).

3.3 Upper boundary of the atmosphere

As no stratospheric chemistry is included in the present version of BCC-AGCM3-Chem, it is necessary to ensure a proper distribution of chemically-active stratospheric species. Concentrations of different tracers (O_3, CH_4, N_2O, NO, NO_2, HNO_3, CO, and N_2O_5) at the top two layers of the model are set to prescribed monthly climatological values, and concentrations from below the top two layers to the tropopause are relaxed at a relaxation

time of 10-days towards the climatology. Climatological values of NO, NO_2, HNO_3, CO and N_2O_5 at the top two layers are extracted from MOZART2 data package available at the Website (https://www2.acom.ucar.edu/gcm/mozart-4), originated from the Study of Transport and Chemical Reactions in the Stratosphere (STARS, Brasseur et al., 1997). Concentrations for the other tracers (O_3, CH_4, and N_2O) at the top two model layers are the zonally-averaged and monthly values from 1850 to 2014 derived from the CMIP6 data package.

3.4 The preindustrial model states

The preindustrial state of BCC-ESM1 is obtained from a piControl simulation of over 600 years in which all forcings including emissions data are fixed at 1850 conditions. The initial state of the piControl simulation itself is obtained through individual spin-up runs of each component of BCC-ESM1 in order for the piControl simulation to run stably and fast to reach its equilibrium. Figures 1(a-c) show the time series of global yearly means of the net energy budget at top of the atmosphere (TOA), near-surface air temperature (TAS), and sea surface temperature (SST) from the piControl simulation for the last 450 years. It shows that the surface climate in BCC-ESM1 nearly reaches its equilibrium after 600 years piControl simulation. The whole system in BCC-ESM1 fluctuates around +0.7 Wm^{-2} net energy flux at TOA without obvious trend in 450 years (Fig. 1a). This level of TOA energy imbalance is close to the average imbalance (1.0 Wm^{-2}) among CMIP5 models (Wild et al., 2013), and do not cause remarkable climate drift in BCC-ESM1. The global mean TAS and SST keep around 288.1 K (Fig. 1b) and 295.05 K (Fig. 1c), respectively. During the last 450 years, there are ($\pm$0.2°K amplitude of TAS and SST) oscillations of centennial scale for the whole globe (Figs. 1b and 1c), which are certainly caused by internal variation of the system.

Figures 2a-2c show the time series of global annual total burdens of SO_2, DMS, and OH in the troposphere (integrated from the surface to 100 hPa) in the last 450 years of the piControl simulation. Without any anthropogenic source, the SO_2 amount in the troposphere nearly keeps the level of 0.0868 Tg in the 450 years of the piControl simulation. Tropospheric DMS varies around the value of 0.116 Tg. Tropospheric OH, as an important gas species oxidizing SO_2 to form SO_4^{2-} (Table 2), keeps at a stable level in the atmosphere. SO_4^{2-} also remains at a stable level of 0.556 Tg in the atmosphere in the whole period of the piControl simulation (Figure 2d). The amounts of BC and OC in the troposphere vary around 0.0395 Tg

and 0.275 Tg (Figures 2e-2f), respectively. Dust and sea salt aerosols are at the level of 22 Tg and 11.7 Tg (Figures 2g-2h), respectively. All those data are close to the global mean concentrations of 0.604 Tg SO_4^{2-}, 0.046 Tg BC, 0.30 Tg OC, 22.18 Tg dust, and 11.73 Tg sea salts in 1850 which are estimated based on the CMIP5 prescribed data in 1850 (Lamarque et al., 2010).

Figure 3 shows the global spatial distributions of annual mean sulfate, organic carbon, black carbon, dust, and sea salt aerosols in the whole atmospheric column averaged for the last 100 years of the piControl simulation of BCC-ESM. We can compare them with CMIP5 recommended concentrations in year 1850, considered as the reference state in the pre-industrial stage. At that time, there are fewer anthropogenic/biomass SO_2 emissions, the SO_4^{2-} over land are evidently smaller than those over oceans especially over the tropical Pacific and Atlantic Oceans, where DMS can be oxidized to SO_2 and then form SO_4^{2-}. There are several centers of high values of black carbon and organic carbon in East and South Asia, Europe, Southeast America, and in the tropical rain forests in Africa and South America. They mainly result from biomass burning including vegetation fires, fuel wood and agricultural burning. Dust aerosols are mainly distributed in North Africa, Central Asia, North China, and Australia, where arid and semi-arid areas locate. Dust emitted from Sahara Desert can be transported to the tropical Atlantic by easterly wind. The sea salt aerosols are mainly distributed over the mid-latitude Southern Oceans, the tropical southern Indian Ocean, and the tropical northern Pacific Ocean, where wind speeds near the sea surface are strong. As shown in Fig. 3, all the spatial distribution patterns of CMIP5-derived sulfate, black carbon, organic carbon, dust, and sea salt aerosols (Lamarque et al., 2010) are well simulated in BCC-ESM1. There are high spatial correlation coefficients, 0.76 for sulfate, 0.77 for black carbon, 0.77 for organic carbon, 0.94 for dust, and 0.94 for sea salts, between CMIP5 data and BCC-ESM1 simulations. Relative lower relations for sulfate, black carbon and organic carbon are possibly caused as different anthropogenic emission sources are used in BCC-ESM1 and to create CMIP5 data. Dust and sea salts belong to natural aerosols and depend on the land and sea surface conditions, so their spatial distributions are easy to be captured and have relatively higher correlations between CMIP5 data and BCC-ESM1 simulations.

4. Evaluation of O_3 and aerosol simulations in the 20th century

The rate of sulfate formation is dependent on the levels of oxidants in the troposphere. O_3 is an important oxidant. So, the evaluation of simulated tropospheric O_3 is helpful to understand the aerosols simulations. BCC-ESM1 is driven by most of the CMIP6-recommended emission data. As shown in Figure 4, the zonal distributions of the total amounts of tropospheric O_3 below 300 hPa to the ground and their changes with time from 1850 to 2014 from the CMIP6-recommend dataset (Table 4) are well simulated by BCC-ESM1. Evident increasing trends since 1850 almost exist in every latitudes, especially in the Northern Hemisphere where the contents of tropospheric O_3 are higher than those in the Southern Hemisphere.

Figure 5 shows the vertical profiles of O_3 simulations with comparison to global ozonesonde observations averaged for the monthly data over 2010-2014 from the World Ozone and Ultraviolet Radiation Data Centre (WOUDC; http://woudc.org/data.php, last access: 24 September 2019) in nine regions which are averaged from 41 global WOUDC sites. The details of WOUDC data may refer to Lu et al. (2019). As shown in Figure 5, BCC-ESM1 well captures the observed ozone vertical structure at all regions. At the lower and middle troposphere (i.e. below 6 km), the model typically shows positive bias within 5 ppbv for the Southern Hemisphere and 10 ppbv for the Northern mid-latitudes, similar to those simulated from many other global atmospheric chemical models (Young et al., 2013, 2018). The model has larger ozone overestimation in the upper troposphere and stratosphere at most regions, at least partly due to the use of prescribed stratospheric ozone as upper boundary conditions and/or errors in modeling ozone exchange between the stratosphere and the troposphere. Global tropospheric ozone burden derived from our simulation is 335 Tg averaged over 2010-2014, in consistent with recent assessment from multi chemistry models (Young et al., 2018).

4.1 Global aerosols trends

Figure 6(a)-(c) show the time series of global total emissions of SO_2, OC, and BC to the atmosphere from natural and anthropogenic sources. Emissions of SO_2 are largely due to industrial production. From 1850 to 1915, SO_2 emissions increased year by year as the Industrial Revolution intensified and expanded. But from 1915 to 1945, the increase trend of

SO_2 emissions became slower as broke out the First and the Second World Wars. After that period, with growing industrial productions, SO_2 emissions increased again and reached a maximum around the end of 1970s. During the 1980s and 2000s, with a substantial decrease of SO_2 emissions in Europe and the United States, the global SO_2 emissions has been decreasing since the 1980s despite the rapid increase of SO_2 emissions in South and East Asia as well as in developing countries in the Southern Hemisphere in recent years (Liu et al., 2009). The OC and BC emissions substantially increased since 1950s just after the Second World War. The global total OC emission in 2010 was nearly twice as much as that in pre-industrial (year 1850) and increased by 18 Tg • yr^{-1}. Anthropogenic black carbon emissions increased from 1 Tg·yr^{-1} in 1850 to nearly 8 Tg·yr^{-1} in 2010.

Anthropogenic SO_2, OC and BC emissions strongly affect the variations of atmospheric concentrations of sulfate, OC, and BC. The global 0.5^ox0.5^o gridded data of CMIP5-recommended aerosols masses with 10-years interval from 1850 to 2000 (Lamarque et al., 2010) provides an important reference to evaluate the aerosol simulations in BCC-ESM1. As shown in Figure 7b-7f, the annual total aerosol burdens of SO_4^{2-}, OC, and BC in the whole atmosphere column as simulated by the BCC-ESM1 20^{th} century historical simulation are generally consistent with the values derived from CMIP5-recommended aerosols concentrations. Due to increasing SO_2 emissions from 1850 to present day (Fig. 6), the global SO_2 burden in the atmosphere increased from 100 Tg in 1850s to 200 Tg in 1980s (Fig. 7a), and has a high correlation coefficient of 0.996 with the anthropogenic emissions (Fig. 6a), as the lifetime of SO_2 is short. The burden directly followed the emission. DMS in the atmosphere is oxidized by OH and NO_3 to form SO_2 (Table 2). Its natural emissions from oceans from 1850 to 2010 in the model are the climatological monthly means (Dentener et al., 2006) from MOZART2 data package. As shown in Fig 7a, the global amount of DMS in the whole atmosphere was about 0.12 Tg during 1850-1900 and decreased to 0.055 Tg in 2010. This decrease trend maybe partly results from the speeded rate of DMS oxidation with global warming, and the loss of DMS gradually exceeds the source of ocean DMS emission to cause a net loss of DMS in the atmosphere since 1910s. Largely driven by SO_2 anthropogenic emissions, the sulfate burden shows three different stages from 1850 to present. In the first period from 1850s to 1900s, the sulfate burden had a weak linear increase. It increased

significantly in the second stage from 1910's to 1940's, and then exploded since 1950's, until the middle 1970s and early 1980s. The sulfate burden then remained nearly stable and even showed slightly decreases as seen from the CMIP5 data. As for global BC and OC burdens, BCC-ESM1 results show continuous increases since 1850s, especially from 1950 to present. From 1910's to 1940's, the CMIP5 data show a slight decrease of BC and OC burdens in the atmosphere.

The dust and sea salt aerosols in the atmosphere are largely determined by the atmospheric circulations and states of the land and ocean surface. We can see that the global dust burden in the atmosphere showed evident increase from 1980 to 2000, which could be partly caused by evident global warming since 1980 and increasing soil dryness resulting in more surface dust to be released in the atmosphere. Their details will be explored in the other paper.

4.2 Global aerosols budgets

We further evaluate global aerosols budgets by comparing a 10-year average of BCC-ESM results from 1990 to 2000 with various studies for sulfate, BC, OC, sea salt, and dust. Their annual total emissions, average atmospheric mass loading, and mean lifetimes are listed in Tables 5 and 6. It is worth emphasizing that the global mean total source and sink for each type of aerosols in BCC-ESM1 are almost balanced.

The global DMS emission from the ocean is 27.4 $Tg(S)\cdot yr^{-1}$ in BCC-ESM. This emission in BCC-ESM is nearly balanced by the gas-phase oxidation of DMS to form SO_2. The DMS burden is 0.12 Tg with a lifetime of 0.78 days, which is within the range of other models reported in the literature. As shown in Table 5, the total SO_2 production averaged for the period of 1991 to 2000 is 76.93 $Tg(S)\cdot yr^{-1}$. A rate of 13.2 $Tg(S)\cdot yr^{-1}$ (about 17%) SO_2 is produced from the DMS oxidation, only 0.1 $Tg(S)\cdot yr^{-1}$ SO_2 from airplane emissions to the atmosphere, and the rest (63.63 $Tg(S)\cdot yr^{-1}$, near 82.7%) from anthropogenic activities and volcanic eruption at surface. The amount of SO_2 produced from the DMS oxidation is in the range of other works (10.0 to 24.7 $Tg(S)\cdot yr^{-1}$) reported in Liu et al (2005). All the SO_2 production is balanced by SO_2 losses by dry and wet deposition, and by gas- and aqueous-phase oxidation. Half of its loss (38.74 $Tg(S)\cdot yr^{-1}$) occurs via its aqueous-phase oxidation to form sulfate. Other losses through dry and wet depositions and gas-phase

525 oxidation to form SO_4^{2-} are also important (Table 2). All the sinks are in the range from the
526 literature (Liu et al., 2005). The global burden of SO_2 in the atmosphere is 0.48 Tg with a
527 lifetime of 1.12 days, consistent with values in literature (Liu et al., 2005).

528 Sulfate aerosol is mainly produced from aqueous-phase SO_2 oxidation (38.73 $Tg(S)\cdot yr^{-1}$)
529 and partly from gaseous phase oxidation of SO_2 (10.32 $Tg(S)\cdot yr^{-1}$), and is largely lost by wet
530 scavenging (49.06 $Tg(S)\cdot y^{r-1}$). The total SO_4^{2-} production in BCC-ESM is at the lower range
531 of values in other models reported in Textor et al. (2006). Its global burden is 1.89 Tg and the
532 lifetime is 4.69 days, which are within the range of 1.71 to 2.43 Tg and 3.3 to 5.4 days in the
533 literatures (Textor et al., 2006; Liu et al., 2012; Liu et al., 2016; Matsui and Mahowald, 2017;
534 Tegen et al., 2019; the value derived from CMIP5 data).

535 Sources of BC and OC are mainly from anthropogenic emissions. Based on the CMIP6
536 data, there are, on average, 7.22 $Tg\cdot yr^{-1}$ BC and 13.91 $Tg\cdot yr^{-1}$ OC from fossil and bio-fuel
537 emissions and 18.38 $Tg\cdot yr^{-1}$ OC from natural emission during the period of 1991 to 2000.
538 Most of them are scavenged through convective and large-scale rainfall processes. The rest
539 returns to the surface by dry deposition. The simulated global BC and OC burdens are 0.13
540 and 0.62 Tg, respectively (Table 6), all close to values of 0.114 Tg BC and 0.69 Tg OC
541 derived from the CMIP5 data, and within the range of 0.11-0.26 Tg BC (Textor et al., 2006;
542 Matsui and Mahowald, 2017; Tegen et al., 2019) and less than the values of 1.25-2.2 Tg OC
543 in other literatures (Textor et al., 2006; Tegen et al., 2019). The simulated BC and OC
544 lifetimes are 6.6 and 5.0 days respectively, and are close to the recent values of 5.0-7.5 days
545 BC and 5.4-6.6 days OC in literatures (Matsui and Mahowald, 2017; Tegen et al., 2019).

546 The emissions of dust and sea salt are mainly determined by winds near the surface. The
547 annual total dust emission in BCC-ESM1 is 2592 Tg yr^{-1}, higher than AeroCom multi-model
548 mean (1840 Tg yr^{-1}, Textor et al., 2006), but comparable to other studies (Chin et al., 2002;
549 Liu et al., 2012; Matsui and Mahowald, 2017). The average dust loading is 22.93 Tg, lower
550 than the value of 35.9 Tg in Ginoux et al. (2001) but slightly higher than the value of 20.41
551 Tg derived from CMIP5 data. The average lifetime for dust particles is 3.23 days that is
552 shorter than the AeroCom mean (4.14 days) and the value of 3.9 days in recent study (Matsui
553 and Mahowald, 2017). The simulated sea salt emission is 4667.2 Tg yr^{-1}, slightly lower than
554 the simulated value in Liu et al. (2012), and substantially lower than the AeroCom mean

555 (16600 Tg yr^{-1}, Textor et al., 2006). The simulated sea salt burdens are 11.89 Tg and close to
556 the CMIP5 data. Their averaged lifetimes are 0.93 days and close to the value in the recent of
557 Matsui and Mahowald (2017) but longer than the AeroCom mean (0.41days, Textor et al.,
558 2006).

559 **4.3 Global aerosol distributions at present day**

560 Figures 8-12 show December-January-February (DJF) and June-July-August (JJA) mean
561 column mass concentrations of sulfate (SO_4^{2-}), OC, BC, Dust, and Sea Salt aerosols averaged
562 for the period of 1991-2000, respectively. Here, BCC-ESM1 simulated results are compared
563 with the CMIP5-recommended data for the same period. Unlike the pre-industrial level of
564 sulfate shown in Fig. 2, sulfate concentrations at present day (Fig. 8) are strongly influenced
565 by anthropogenic emissions, and have maximum concentrations in the industrial regions (e.g.,
566 East Asia, Europe, and North America). Their seasonal variations are distinct and are
567 characterized by high concentrations in boreal summer and low concentrations in boreal
568 winter. These spatial distributions simulated by BCC-ESM1 are well consistent with the
569 CMIP5 data, with spatial correlation coefficients in DJF and JJA reaching 0.92 and 0.83
570 (Figure 13), respectively. The deviation of the spatial pattern in BCC-ESM1 is less from the
571 CMIP5 data in DJF but larger in JJA (Figure 13).

572 Unlike sulfate whose maximum concentrations are mainly distributed between 60°N
573 and the equator, peaking concentrations of BC and OC as shown in Figs. 9 and 10 are located
574 near the tropics in the biomass burning regions (e.g., the maritime continent, Central Africa,
575 South America), and their seasonal variations from DJF to JJA are evidently weaker than
576 those of sulfate except in South America. In boreal summer, there are centers of high values
577 in the industrial regions in the Northern Hemisphere mid-latitudes (i.e., East Asia, South Asia,
578 Europe, and North America). These main features of spatial and seasonal variations in CMIP5
579 data are well captured by BCC-ESM1, and the BCC-ESM1 vs. CMIP5 spatial correlation
580 coefficients (Figure 13) are 0.90 (OC in DJF), 0.91 (BC in DJF), 0.91 (OC in JJA) and 0.92
581 (BC in JJA). There are less deviations of spatial pattern for OC in DJF and JJA, but larger
582 deviation for BC from CMIP5 data (Figure 13).

583 As show in Figure 11, dust concentrations in the atmosphere show largest values over
584 strong source regions such as Northern Africa, Southwest and Central Asia, and Australia,

585 and over their outflow regions such as the Atlantic and the western Pacific. In DJF, the
586 CMIP5 data shows centers of high concentrations over East Asia and Central North America,
587 but both centers are missing in BCC-ESM1. However, these two high-value centers in the
588 CMIP5 data may not be true, since frozen soils in these areas in winter lead to unfavorable
589 conditions for soil erosion by winds. The spatial correlation coefficients between CMIP5 and
590 BCC-ESM1 remain high: 0.95 in JJA and 0.88 in DJF (Figure 13). Small deviations of spatial
591 pattern for dust simulations in BCC-ESM1 show less magnitude of dust maximums against
592 with CMIP5 data (Figure 13).

593 As shown in Figure 12, high sea salt concentrations are generally over the storm track
594 regions over the oceans, e.g., mid-latitudes in the Northern Oceans in DJF and the Southern
595 Ocean in JJA where wind speeds and thus sea salt emissions are higher. In addition, there is a
596 belt of high sea salt concentrations in the subtropics of both hemispheres where precipitation
597 scavenging is weak. Their spatial distributions in BCC-ESM1 are consistent with the CMIP5
598 data with correlation coefficients of 0.92 in JJA and 0.90 in DJF (Figure 13). The spatial
599 deviations of sea salt are much closer to CMIP5 data than those of sulfate, OC, BC, and dust
600 distributions (Figure 13).

601 Figure 14 shows vertical distributions of zonally-averaged annual mean concentrations
602 of sulfate, organic carbon, black carbon, dust, and sea salt aerosols in the period of 1991-2000.
603 Both BCC-ESM1 and CMIP5 results show that strong sulfur, OC, and BC emissions in the
604 industrial regions of the Northern Hemisphere mid-latitudes can rise upward and be
605 transported towards the North Pole in the mid- to upper troposphere. Most of OC, BC, and
606 dust aerosols are confined below 500 hPa, while sulfate can be transported to higher altitudes.
607 Sea salt aerosols are mostly confined below 700 hPa, as the particles are large in size and
608 favorable for wet removal and gravitational settling towards the surface. It can be seen that
609 BCC-ESM1 tends to simulate less upward transport of aerosols than the CMIP5 data, likely
610 reflecting the omission of deep convection transport of tracers in BCC-ESM1.

611 The CMIP5 data used here are mainly from model simulations. We will further evaluate
612 the BCC-ESM1 model results with ground observations. Annual mean SO_4^{2-}, BC and OC
613 aerosol observations from the Interagency Monitoring of Protected Visual Environments
614 (IMPROVE) sites over 1990-2005 in the United States

615 (http://vista.cira.colostate.edu/IMPROVE/) and from the European Monitoring and Evaluation
616 Programme (EMEP) (http://www.emep.int) sites over 1995-2005 are used. As shown in
617 Figure 15a and 15b, the BCC-ESM simulated sulfate concentrations are in general
618 comparable to the EMEP observations in Europe, but are systematically by about 1 μg m^{-3}
619 higher than the U.S. IMPROVE observations. As for BC, there are large model biases at both
620 European and U.S. sites (Figs. 15c and 15d), especially BCC-ESM overestimates BC
621 concentrations at the IMPROVE sites. The observed OC concentrations are slightly
622 overestimated for IMPROVE sites but systematically underestimated for EMEP sites. Some
623 statistical features for simulated concentrations versus EMEP and IMPROVE observations are
624 listed in Table 7. These comparisons are overall fairly reasonable considering the
625 uncertainties in emissions and the coarse model resolution.

626 We then evaluate the simulated BC concentrations from BCC-ESM1 with the HIAPER
627 (High-Performance Instrumented Airborne Platform for Environmental Research)
628 Pole-to-Pole Observations (HIPPO) (Wofsy et al., 2011). The HIPPO campaign provided
629 observations of black carbon concentration profiles over Pacific Ocean and North America
630 between 2009 and 2011. Following Tilmes et al. (2016), model results here are sampled along
631 the HIPPO flight tracks and then averaged to different latitude and altitude bands for
632 comparison. As shown in Figure 16, BCC-ESM1 and HIPPO aircraft observations shows
633 reasonable agreement in terms of the spatial distributions and seasonal variations of BC levels.
634 BCC-ESM1 generally reproduces the observed hemispheric gradients of BC, i.e. the larger
635 burden in the NH compared to the SH, in consistent with Figures 10 and 14. The model shows
636 large overestimations of BC observations over the tropics, which is also found in the
637 CAM4-chem global chemical model (Tilmes et al., 2016).

638 **4.4 Aerosol Optical Properties**

639 Aerosol optical depth (AOD) is an indicator of the reduction in incoming solar
640 radiation (at a particular wavelength) due to scattering and absorption of sunlight by aerosols.
641 In this study, we calculate the AOD at 550 nm for all aerosols including sulfate, BC, organic
642 carbon, sea salt and dust as the product of aerosol dry mass concentrations, aerosol water
643 content, and their specific extinction coefficients. The total AOD is calculated by summing

644 the AOD in each model layer for each aerosol species using the assumption that they are
645 externally mixed. The AOD observations retrieved from MODIS and MISR over the period of
646 1997-2003, and from AERONET over the period of 1998–2005 (http://aeronet.gsfc.nasa.gov)
647 are used to evaluate the averaged AOD at 550 nm in BCC-ESM. Figure 17 shows averages of
648 MISR and MODIS AOD with corresponding averages from BCC-ESM. The BCC-ESM1
649 simulated AOD generally captures the spatial distribution of MISR and MODIS retrievals.
650 The model overestimates AOD over East China. It also systematically underestimates the
651 MODIS observations in the Southern Hemisphere, but is closer to MISR observations. Figure
652 18 shows multi-years annual means of BCC-ESM1 simulated AOD values versus
653 observations from AERONET over the period of 1998–2005. The basic pattern of modeled
654 global AOD is similar to that of observations and their spatial correlation reaches 0.56. Large
655 values of AOD are mainly distributed in land continents such as North African, South Asia,
656 East Asia, Europe, and eastern part of North America. Figures 19a-19d present scatter plots of
657 observed versus simulated multi-year monthly mean AOD at those sites of AERONET in
658 Europe, North America, East Asia, and South Asia over the period of 1998-2005, respectively.
659 Model simulated monthly AOD generally agrees with observations within a factor of 2 for
660 most sites. BCC-ESM slightly overestimates the AOD in European and North American sites.
661 In those regions, BCC-ESM also slightly overestimates MODIS and MISR AOD observations
662 (Fig. 17).

663 ## 5. Summary and discussions

664 This paper presents a primary evaluation of aerosols simulated in version 1 of the Beijing
665 Climate Center Earth System Model (BCC-ESM1) with the implementation of the interactive
666 atmospheric chemistry and aerosol based on the newly developed BCC-CSM2. Global
667 aerosols (including sulfate, organic carbon, black carbon, dust and sea salt) and major
668 greenhouse gases (e.g., O_3, CH_4, N_2O) in the atmosphere can be interactively simulated when
669 anthropogenic emissions are provided to the model. Concentrations of all aerosols in
670 BCC-ESM1 are determined by the processes of advective transport, emission, gas-phase
671 chemical reactions, dry deposition, gravitational settling, and wet scavenging by clouds and
672 precipitation. The nucleation and coagulation of aerosols are ignored in the present version of
673 BCC-ESM1. Effects of aerosols on radiation, cloud, and precipitation are fully included.

We evaluate the performance of BCC-ESM1 in simulating aerosols and their optical properties in the 20th century following CMIP6 historical simulation according to the requirement of the AerChemMIP. It is forced with anthropogenic emissions evolving from 1850 to 2014 but some WMGHGs such as CH_4, N_2O, CO_2, CFC11 and CFC12 are prescribed using CMIP6 prescribed concentrations (to replace prognostic values of CH_4 and N_2O from the chemistry scheme). Both direct and indirect effects of aerosols are considered in BCC-ESM1. Initial conditions of the CMIP6 historical simulation are obtained from a 600-year piControl simulation in the absence of anthropogenic emissions, which well captures the pre-industrial concentrations of SO_4^{2-}, organic carbon (OC), black carbon (BC), dust, and sea salt aerosols and are consistent with the CMIP5 recommended concentrations for the year 1850. With the CMIP6 anthropogenic emissions of SO_2, OC, and BC from 1850 to 2014 and their natural emissions implemented in BCC-ESM1, the model simulated SO_4^{2-}, BC, and OC aerosols in the atmosphere are highly correlated with the CMIP5-recommended data. The long-term trends of CMIP5 aerosols from 1850 to 2000 are also well simulated by BCC-ESM1. Global budgets of aerosols were evaluated through comparisons of BCC-ESM1 results for 1990-2000 with reports in various literatures for sulfate, BC, OC, sea salt, and dust. Their annual total emissions, atmospheric mass loading, and mean lifetimes are all within the range of values reported in relevant literature. Evaluations of the spatial and vertical distributions of BCC-ESM1 simulated present-day SO_4^{2-}, OC, BC, Dust, and sea salt aerosol concentrations against the CMIP5 datasets and in-situ measurements of surface networks (IMPROVE in the U.S. and EMEP in Europe), and HIPPO aircraft observations indicate good agreement among them. The BCC-ESM1 simulates weaker upward transport of aerosols from the surface to the middle and upper troposphere (with reference to CMIP5-recommended data), likely reflecting a lack of deep convection transport of chemical species in the present version of BCC-ESM1. The AOD at 550 nm for all aerosols including sulfate, BC, OC, sea salt, and dust aerosols was further compared with the satellite AOD observations retrieved from MODIS and MISR and surface AOD observations from AERONET. The BCC-ESM1 model results are overall in good agreement with these observations within a factor of 2. All these comparisons demonstrate the success of the implementation of interactive aerosol and atmospheric chemistry in BCC-ESM1.

This work has only evaluated the ability of BCC-ESM1 to simulate aerosols. The variations of aerosols especially for sulfate are related to other gaseous tracers such as OH and NO_3 (Table 2), which are determined by the MOZART2 gaseous chemical scheme as implemented in BCC-ESM1, and require further evaluation. As limited length of the text, the other optical feature of aerosols such as extinction coefficients, single scattering albedo and asymmetry parameters, and even their feedbacks on radiation and global temperature change will be explored in the other paper. O_3 is evaluated in this work. Other GHGs such as CH_4 and N_2O concentrations can be simulated when forced with emissions and their simulations also need to be evaluated in future.

6. Code and data availability

Source codes of BCC-ESM1 model are freely available upon request addressed to Tongwen Wu (twwu@cma.gov.cn). Model output of BCC CMIP6 AerChemMIP simulations described in this paper is distributed through ESGF and freely accessible through the ESGF data portals after registration. Details about ESGF are presented on the CMIP Panel website at http://www.wcrp-climate.org/index.php/wgcm-cmip/about-cmip.

Author contributions

Tongwen Wu led the BCC-ESM1 development. All other co-authors have contributions to it. Fang Zhang and Jie Zhang designed the experiments and carried them out. Tongwen Wu, Laurent Li, Lin Zhang, Xiaohong Liu, Aixue Hu, and Jun Wang wrote the final document with contributions from all other authors.

Acknowledgements

This work was supported by The National Key Research and Development Program of China (2016YFA0602100). All the figures are created by the NCAR Command Language (Version 6.6.2) [Software].

References

Albani, S., Mahowald, N. M., Perry, A. T., Scanza, R. A., Zender, C. S., Heavens, N. G., Maggi, V., Kok, J. F., and Otto-Bliesner, B. L.: Improved dust representation in the

734 Community Atmosphere Model, J. Adv. Model. Earth Syst., 6, 541–570,
735 doi:10.1002/2013MS000279, 2014.
736 Albrecht, B.: Aerosols, cloud microphysics, and fractional cloudiness, Science, 245, 1227–
737 1230, 1989.
738 Arora, V., Boer, G., Friedlingstein, P., Eby, M., Jones, C., Christian, J., Bonan, G., Bopp, L.,
739 Brovkin, V., Cadule, P., Hajima, T., Ilyina, T., Lindsay, K., Tjiputra, J., and Wu, T.:
740 Carbon-concentration and carbon-climate feedbacks in CMIP5 Earth system models. J.
741 Climate, 26, 5289–5314, 2013.
742 Austin, J., Butchart, N., and Shine, K. P.: Possibility of an Arctic ozone hole in a
743 doubled-CO2 climate, Nature, 360, 221–225, 1992
744 Barth, M.C., Rasch, P.J., Kiehl, J.T., Benkowitz, C.M., and Schwartz, S.E.: Sulfur chemistry
745 in the National Center for Atmospheric Research Community Climate Model:
746 Description, evaluation, features, and sensitivity to aqueous chemistry. J. Geophys. Res.,
747 105, D1, 1387-1415, 2000.
748 Bey I., Jacob, D. J., Yantosca, R. M., Logan, J. A., Field, B., Fiore, A. M., Li, Q., Liu, H.,
749 Mickley, L. J., and Schultz, M.: Global modeling of tropospheric chemistry with
750 assimilated meteorology: Model description and evaluation, J. Geophys. Res., 106,
751 23,073-23,096, 2001
752 Boucher, O., Lohmann, U.: The sulphate-CCN-cloud albedo effect – a sensitivity study with
753 two general circulation models, Tellus 47B, 281–300, 1995.
754 Brasseur, G. P., Hauglustaine, D. A., Walters, S., Rasch, P. J., Mu¨ller, J.-F., Granier, C., and
755 Tie, X. X.: MOZART, a global chemical transport model for ozone and related chemical
756 tracers: 1. Model description, J. Geophys. Res., 103, 28,265– 28,289, 1998.
757 Brasseur, G. P., Tie, X. X., Rasch, P. J., and Lefèvre, F.: A three‐dimensional simulation of
758 the Antarctic ozone hole: Impact of anthropogenic chlorine on the lower stratosphere and
759 upper troposphere, J. Geophys. Res., 102, 8909–8930, 1997.
760 Cariolle, D., Lasserre-Bigorry, A., and Royer, J.-F.: A general circulation model simulation of
761 the springtime Antarctic ozone decrease and its impact on midlatitudes, J. Geophys. Res.,
762 95, 1883–1898, 1990.
763 Chen, C., and Cotton, W. R.: The physics of the marine stratocumulus-capped mixed layer, J.
764 Atmos. Sci., 44 (50), 2951–2977, 1987.
765 Chin, M., Ginoux, P., Kinne, S., Torres, O., Holben, B.N., Duncan, B.N., Martin, R.V., Logan, J.A.,

766 Higurashi, A., Naka-jima, T.: Tropospheric aerosol optical thickness from the GOCART
767 model and comparisons with satellite and Sun photometer measurements. J. Atmos.
768 Sci. 59:461–483, 2002.
769 Chuang, C. C., Penner, J. E., Taylor, K. E., Grossman, A. S., and Walton, J. J.: An assessment
770 of the radiative effects of anthropogenic sulfate, J. Geophys. Res., 102, 3761–3778,
771 1997.
772 Collins, W. J., Lamarque, J.–F., Schulz, M., Boucher, O., Eyring, V., Hegglin, M. I.,
773 Maycock, A., Myhre, G., Prather, M., Shindell, D., Smith, S. J.: AerChemMIP:
774 quantifying the effects of chemistry and aerosols in CMIP6, Geosci. Model Dev., 10,
775 585–607, 2017.
776 Collins, W. D., Rasch, P. J., Boville, B. A., Hack, J. J., McCaa, J. R., Williamson, D. L,.
777 Kiehl, J. T., Briegleb, B. P., Bitz, C., Lin, S.-J., Zhang, M., and Dai, Y.: Description of
778 the NCAR Community Atmosphere Model (CAM3). Nat. Cent. for Atmos. Res.,
779 Boulder, Colo., 2004.
780 Cooke, W.F., Wilson, J.J.N.: A global black carbon aerosol model. J. Geophys. Res. Atmos.
781 101, 19395–19409, 1996.
782 Cunnold, D., Alyea, F., Phillips, N., Prinn, R.: A three-dimensional dynamical-chemical
783 model of atmospheric ozone, J. Atmos. Sci., 32, 170-194, 1975.
784 Dentener, F., Kinne, S., Bond, T., Boucher, O., Cofala, J., Generoso, S., Ginoux, P., Gong, S.,
785 Hoelzemann, J. J., Ito, A., Marelli, L., Penner, J. E., Putaud, J.-P., Textor, C., Schulz, M.,
786 van der Werf, G. R., and Wilson, J.: Emissions of primary aerosol and precursor gases in
787 the years 2000 and 1750 prescribed data-sets for AeroCom, Atmos. Chem. Phys., 6,
788 4321–4344, doi:10.5194/acp-6-4321-2006, 2006.
789 Eyring, V., Bony, S., Meehl, G. A., Senior, C. A., Stevens, B., Stouffer, R. J., and Taylor, K.
790 E.: Overview of the Coupled Model Intercomparison Project Phase 6 (CMIP6)
791 experimental design and organization, Geosci. Model Dev., 9, 1937–1958,
792 doi:10.5194/gmd-9-1937-2016, 2016.
793 Feichter, J., Kjellstrom, E., Rodhe, H., Dentener, F., Lelieveldi, J., Roelofs, G.-J.: Simulation
794 of the tropospheric sulfur cycle in a global climate model, 30: 1693-1707, 1996.
795 Ghan, S. J. and Easter, R. C.: Impact of cloud-borne aerosol representation on aerosol direct
796 and indirect effects, Atmos. Chem. Phys., 6, 4163–4174, 2006.
797 Ginoux, P., M. Chin, I. Tegen, J. M. Prospero, B. Holben, O. Dubovik, and S.-J. Lin (2001),

798 Sources and distributions of dust aerosols simulated with the GOCART model, J.
799 Geophys. Res., 106, 20,255 – 20,274.
800 Giorgi, F., and Chameides, W. L.: The rainout parameterization in a photochemical model, J.
801 Geophys. Res., 90, 7872–7880, 1985.
802 Guenther, A. B., Jiang, X., Heald, C. L., et al.: The Model of Emissions of Gases and
803 Aerosols from Nature Version 2.1 (MEGAN2.1): An Extended and Updated Framework
804 for Modeling Biogenic Emissions. Geoscientific Model Development 5(6): 1471–1492,
805 2012.
806 Guenther, A., Baugh, B. Brasseur, G., Greenberg, J., Harley, P., Klinger, L,. Serca, D., and
807 Vierling, L.: Isoprene emission estimates and uncertainties for the Central African
808 EXPRESSO study domain, J. Geophys. Res., 104(D23), 30,625–30,639, 1999.
809 Hoesly, R. M., Smith, S. ., Feng, L., Klimont, Z., Janssens-Maenhout, G., Pitkanen, T.,
810 Seibert, J. J., Vu, L., Andres, R. J., Bolt, R. M., Bond, T. C., Dawidowski, L., Kholod, N.,
811 Kurokawa, J., Li, M., Liu, L., Lu, Z., Moura, M. C. P., O'Rourke, R. R., and Zhang Q.:
812 Historical (1750–2014) anthropogenic emissions of reactive gases and aerosols from the
813 Community Emission Data System (CEDS), Geosci. Model Dev., 11, 369-408, 2018
814 Horowitz, L.W., Walters, S., Mauzerall, D. L., Emmons, L. K., Rasch, P. J., Granier, C., Tie,
815 X., Lamarque, J.-F., Schultz, M. G., Tyndall, G. S., Orlando, J. J., Brasseur, G. P.: A
816 global simulation of tropospheric ozone and related tracers: Description and evaluation
817 of MOZART, version 2, J. Geophys. Res., 108(D24), 4784, doi:10.1029/2002JD002853,
818 2003.
819 Horowitz, L. W.: Past, present, and future concentrations of tropospheric ozone and aerosols:
820 Methodology, ozone evaluation, and sensitivity to aerosol wet removal, J. Geophys. Res.,
821 111, D22211, doi:10.1029/2005JD006937, 2006.
822 Hoffman, F. M., Randerson, J. T., Arora, V. K., Bao, Q., Cadule, P., Ji, D., Jones, C. D.,
823 Kawamiya, M., Khatiwala, S., Lindsay, K., Obata, A., Shevliakova, E., Six, K. D.,
824 Tjiputra, J. F., Volodin, E. M., and Wu, T.: Causes and implications of persistent
825 atmospheric carbon dioxide biases in Earth System Models, J. Geophys. Res. Biogeosci.,
826 119, 141–162, doi:10.1002/2013JG002381, 2014.
827 Holtslag, A. A. M., and Boville, B. A.: Local versus nonlocal boundary-layer diffusion in a
828 global climate model, J. Climate, 6, 1825–1842, 1993.
829 Jacobson, M.Z.: Investigating cloud absorption effects: global absorption properties of black

carbon, tar balls, and soil dust in clouds and aerosols. J. Geophys. Res. 117, D06205, 2012.

Jones, C.D., Arora, V., Friedlingstein, P., Bopp, L., Brovkin, V., Dunne, J., Graven, H., Hoffman, F., Ilyina, T., John, J. G., Jung, M., Kawamiya, M., Koven, C., Pongratz, J., Raddatz, T., Randerson, J. T., and Zaehle, S.: C4MIP – The Coupled Climate–Carbon Cycle Model Intercomparison Project: experimental protocol for CMIP6, Geosci. Model Dev., 9, 2853–2880, doi:10.5194/gmd-9-2853-2016, 2016.

Lamarque, J.-F., Shindell, D. T., Josse, B., Young, P. J., Cionni, I., Eyring, V., Bergmann, D., Cameron-Smith, P., Collins,W. J., Doherty, R., Dalsoren, S., Faluvegi, G., Folberth, G., Ghan, S. J., Horowitz, L. W., Lee, Y. H., MacKenzie, I. A., Nagashima, T., Naik, V., Plummer, D., Righi, M., Rumbold, S. T., Schulz, M., Skeie, R. B., Stevenson, D. S., Strode, S., Sudo, K., Szopa, S.,Voulgarakis, A., and Zeng, G.: The Atmospheric Chemistry and Climate Model Intercomparison Project (ACCMIP): overview and description of models, simulations and climate diagnostics, Geosci. Model Dev., 6, 179–206, doi:10.5194/gmd-6-179-2013, 2013.

Lamarque, J.-F., Emmons, L. K., Hess, P. G., Kinnison, D. E., Tilmes, S., Vitt, F., Heald, C. L., Holland, E. A., Lauritzen, P. H., Neu, J., Orlando, J. J., Rasch, P. J., and Tyndall, G. K.: CAM-chem: description and evaluation of interactive atmospheric chemistry in the Community Earth System Model, Geosci. Model Dev., 5, 369–411, 2012

Lamarque, J.-F., Bond, T. C., Eyring, V., Granier, C., Heil, A., Klimont, Z., Lee, D., Liousse, C., Mieville, A., Owen, B., Schultz, M. G., Shindell, D., Smith, S. J., Stehfest, E., Van Aardenne, J., Cooper, O. R., Kainuma, M., Mahowald, N., McConnell, J. R., Naik, V., Riahi, K., and van Vuuren, D. P.: Historical (1850–2000) gridded anthropogenic and biomass burning emissions of reactive gases and aerosols: methodology and application, Atmos. Chem. Phys., 10, 7017-7039, https://doi.org/10.5194/acp-10-7017-2010, 2010.

Lohmann, U., Feichter, J., Penner, J. E., and Leaitch, W. R.: Indirect effect of sulfate and carbonaceous aerosols: A mechanistic treatment. J. Geophys. Res, 105, 12193–12206, 2000

Li, W., Zhang, Y., Shi, X., Zhou, W., Huang, A., Mu, M., Qiu, B., JI, J.: Development of the Land Surface Model BCC_AVIM2.0 and Its Preliminary Performance in LS3MIP/CMIP6, J. Meteor. Res., 33(5), doi: 10.1007/s13351-019-9016-y, 2019.

Liu, X. H., Penner, J. E., and Herzog, M.: Global modeling of aerosol dynamics: Model

862 description, evaluation, and interactions between sulfate and nonsulfate aerosols, J.
863 Geophys. Res.-Atmos., 110, D18206, doi:10.1029/2004jd005674, 2005.
864 Liu, X., Easter, R.C. Ghan, S.J., Zaveri, R., Rasch, P., Shi, X., Lamarque, J.-F., Gettelman, A.,
865 Morrison, H., Vitt, F., Conley, A., Park, S., Neale, R., Hannay, C., Ekman, A.M., Hess,
866 P., Mahowald, N., Collins, W., Iacono, M.J., Bretherton, C.S., Flanner, M.G., and
867 Mitchell, D.: Toward a Minimal Representation of Aerosols in Climate Models:
868 Description and Evaluation in the Community Atmosphere Model CAM5.
869 Geos.Model.Dev. 5(3):709-739. 2012.
870 Liu, X., Ma, P. -L., Wang, H., Tilmes, S., Singh, B., Easter, R. C., Ghan, S. J., and Rasch, P.
871 J.: Description and evaluation of a new four-mode version of the Modal Aerosol Module
872 (MAM4) within version 5.3 of the Community Atmosphere Model, Geosci. Model Dev.,
873 9, 505–522, https://doi.org/10.5194/gmd-9-505-2016, 2016.
874 Liu, J., Mauzerall, D.L., Horowitz, L.W., Ginoux, P., Fiore, A.M.: Evaluation intercontinental
875 transport of fine aerosols: (1) methodology, global aerosol distribution and optical depth.
876 Atmos Environ 43:4327–4338, 2009.
877 Lu, X., Zhang, L., Wu, T., Long, M., Wang, J., Jacob, D., Zhang F., Zhang, J., Eastham, S.,
878 Hu, L., Zhu, L., Liu, X., an Wei, M.: Development of the global atmospheric general
879 circulation-chemistry model BCC-GEOS-Chem v1.0: model description and evaluation,
880 submitted to Geos.Model.Dev.
881 Mahowald, N., Lamarque, J.-F., Tie, X., and Wolff, E.: Sea salt aerosol response to climate
882 change: last glacial maximum, preindustrial and doubled carbon dioxide climates, J.
883 Geophys. Res., 111, D05303, doi:10.1029/2005JD006459, 2006.
884 Martin, R. V., et al.: Interpretation of TOMS observations of tropical tropospheric ozone with
885 a global model and in situ observations, J. Geophys. Res., 107(D18), 4351,
886 doi:10.1029/2001JD001480, 2002.
887 Matsui, H., and Mahowald, N.: Development of a global aerosol model using a
888 two-dimensional sectional method: 2. Evaluation and sensitivity simulations, J. Adv.
889 Model. Earth Syst., 9, 1887–1920, doi:10.1002/2017MS000937, 2017.
890 Mora, C., Wei, C.-L., Rollo, A., Amaro, T., Baco, A.R., Billett, D., Bopp, L., Chen, Q.,
891 Collier, M., Danovaro, R., Gooday, A.J., Grupe, B.M., Halloran, P.R., Ingels, J., Jones,
892 D.O.B., Levin, L.A., Nakano, H., Norling, K., Ramirez-Llodra, E., Rex, M., Ruh, H.A.,
893 Smith, C.R., Sweetman, A.K., Thurber, A.R., Tjiputra, J. F., Usseglio, P., Watling, L.,

Wu, T., Yasuhara, M.: Biotic and human vulnerability to projected ocean biogeochemistry change over the 21st century, PLoS Biol 11(10): e1001682. doi:10.1371/journal.pbio.1001682, 2013.

NCAR Command Language (Version 6.6.2) [Software], Boulder, Colorado: UCAR/NCAR/CISL/TDD. http://dx.doi.org/10.5065/D6WD3XH5, 2019.

Neale, R. B., et al.: Description of the NCAR Community Atmosphere Model (CAM 4.0), NCAR Tech. Note, TN-485, pp. 212, Natl. Cent. for Atmos. Res., Boulder, Colo., 2010

Neu, J. L. and Prather, M. J.: Toward a more physical representation of precipitation scavenging in global chemistry models: cloud overlap and ice physics and their impact on tropospheric ozone, Atmos. Chem. Phys. Discuss., 11, 24413–24466, doi:10.5194/acpd-11-24413-2011, 2011.

Olivier, J.G.J., Bouwman, A.F., Van der Maas, C.W.M., Berdowski, J.J.M., Veldt, C., Bloos, J.P.J., Visschedijk, A.J.H., Zandveld, P.Y.J., Haverslag, J.L., Description of EDGAR Version 2.0: A set of global emission inventories of greenhouse gases and ozone depleting substances for all anthropogenic and most natural sources on a per country basis and on 1° x1° grid. RIVM Techn. Report nr. 771060002, TNO-MEP report nr. R96/119.Nat. Inst. Of Public Health and the Environment/ Netherlands Organisation for Applied Scientific Research, Bilthoven, 1996.

Peng, Y., and Lohmann, U.: Sensitivity study of the spectral dispersion of the cloud droplet size distribution on the indirect aerosol effect, Geophys. Res. Lett., 30(10), 1507, doi:10.1029/2003GL017192, 2003.

Price, C., and Rind, D.: A simple lightning parameterization for calculating global lightning distributions, J. Geophys. Res., 97, 9919-9933, 1992.

Quaas, J., Boucher, O., and Lohmann, U.: Constraining the total aerosol indirect effect in the LMDZ and ECHAM4 GCMs using MODIS satellite data. Atmos Chem Phys 6,947–955, 2006.

Sander, S., Friedl, R. R., Ravishankara, A. R., et al.: Chemical Kinetics and Photochemical Data for Use in Atmospheric Studies, Evaluation Number 14, JPL Publication 02-25, NASA, Jet Propulsion Laboratory, California Institute of Technology, Pasadena, CA, 2003.

Schlesinger, M. E., Mintz, Y.: Numerical simulation of ozone production, transport and

925 distribution with a global atmospheric general circulation model, J.Atmos.Sci., 36:
926 1325-1361, 1979.
927 Shindell, D.T., Horowitz, L.W., Schwarzkopf, M.D.: Composition Models in Climate
928 Projections Based on Emissions Scenarios for Long-Lived and Short-Lived Radiatively
929 Active Gases and Aerosols. H.Levy II, D.T. Shindell, A.Gilliland, M.D.Schwarzkopf,
930 L.W.Horowitz, (eds.) .A Report by the U.S.Climate Change Science Program and the
931 Subcommittee on Global Change Research, Washington, D.C., 2008
932 Solomon, S.: Stratospheric ozone depletion: A review of concepts and history, Reviews of
933 Geophysics, 37, 275–316, 1999.
934 Taylor, K.E., Stouffer, R. J., Meehl, G. A.: An overview of CMIP5 and the experiment design,
935 Bull. Am. Meteorol. Soc. 93, 485-498, 2012.
936 Tegen, I., Neubauer, D., Ferrachat, S., Siegenthaler-Le Drian, C., Bey, I., Schutgens, N., Stier,
937 P., Watson-Parris, D., Stanelle, T., Schmidt, H., Rast, S., Kokkola, H., Schultz, M.,
938 Schroeder, S., Daskalakis, N., Barthel, S., Heinold, B., and Lohmann, U.: The global
939 aerosol–climate model ECHAM6.3–HAM2.3 – Part 1: Aerosol evaluation, Geosci.
940 Model Dev., 12, 1643–1677, https://doi.org/10.5194/gmd-12-1643-2019, 2019.
941 Textor, C., Schulz, M., Guibert, S., Kinne, S., Balkanski, Y., Bauer, S., Berntsen, T., Berglen,
942 T., Boucher, O., Chin, M., Dentener, F., Diehl, T., Easter, R., Feichter, H., Fillmore, D.,
943 Ghan, S., Ginoux, P., Gong, S., Grini, A., Hendricks, J., Horowitz, L., Huang, P., Isaksen,
944 I., Iversen, I., Kloster, S., Koch, D., Kirkevåg, A., Kristjansson, J. E., Krol, M., Lauer, A.,
945 Lamarque, J. F., Liu, X., Montanaro, V., Myhre, G., Penner, J., Pitari, G., Reddy, S.,
946 Seland, Ø., Stier, P., Takemura, T., and Tie, X.: Analysis and quantification of the
947 diversities of aerosol life cycles within AeroCom, Atmos. Chem. Phys., 6, 1777–1813,
948 https://doi.org/10.5194/acp-6-1777-2006, 2006.
949 Thomason, L. W., Ernest, N., Millán, L., Rieger, L., Bourassa, A., Vernier, J. P., Manney, G.,
950 Luo, B.P., Arfeuille, F., Peter, T.: A global space‐based stratospheric aerosol
951 climatology: 1979-2016. Earth System Science Data, 10(1), 469–492, doi:
952 10.5194/essd-10-469-2018, 2018.
953 Tie, X., Brasseur, G., Emmons, L., Horowitz, L., and Kinnison, D.: Effects of aerosols on
954 tropospheric oxidants: A global model study, J. Geophys. Res., 106, 2931– 2964, 2001.
955 Tie, X., Madronich, S., Walters, S., Edwards, D., Ginoux, P., Mahowald, N., Zhang, R., Luo,
956 C., and Brasseur, G.: Assessment of the global impact of aerosols on tropospheric

957 oxidants, J. Geophys. Res., 110, D03204, doi:10.1029/2004JD005359, 2005.
958 Tilmes, S., Lamarque, J.-F., Emmons, L. K., Kinnison, D. E., Marsh, D., Garcia, R. R., Smith,
959 A. K., Neely, R. R., Conley, A., Vitt, F., Val Martin, M., Tanimoto, H., Simpson, I.,
960 Blake, D. R., and Blake, N.: Representation of the Community Earth System Model
961 (CESM1) CAM4-chem within the Chemistry-Climate Model Initiative (CCMI),
962 Geoscientific Model Development, 9, 1853-1890, 2016.
963 Todd-Brown, K.E.O., Randerson, J.T., Hopkins, F., Arora, V., Hajima, T., Jones, C.,
964 Shevliakova, E., Tjiputra, J., Volodin, E., Wu, T., Zhang, Q., Allison, S.D.: Changes in
965 soil organic carbon storage predicted by Earth system models during the 21st century,
966 Biogeosciences, 11, 2341-2356, 2014.
967 Wang, J., Hoffmann, A. A., Park, R., Jacob, D. J., and Martin, S. T.: Global distribution of
968 solid and aqueous sulfate aerosols: effect of the hysteresis of particle phase transitions, J.
969 Geophys. Res., 113, D11206, Doi:11210.11029/12007JD009367, 2008a.
970 Wang, J., Jacob, D. J., and Martin, S. T.: Sensitivity of sulfate direct climate forcing to the
971 hysteresis of particle phase transitions, J. Geophys. Res., 113, D11207,
972 doi:11210.11029/12007JD009368, 2008b.
973 Wesely, M. L.: Parameterization of surface resistance to gaseous dry deposition in
974 regional-scale numerical models, Atmos. Environ., 23, 1293–1304, 1989.
975 Wild, M., Folini, D., Schar, C., Loeb, N., Dutton, E.G., Konig-Langlo, G.: The global energy
976 balance from a surface perspective, Climate Dynamics, 40: 3107-3134, 2013.
977 Williamson, D. L., and Rasch, P. J.: Two-dimensional semi-Lagrangian transport with
978 shapepreserving interpolation, Mon. Wea. Rev., 117, 102–129, 1989.
979 Wofsy, S. C. and the HIPPO team: HIAPER Pole-to-Pole Observations (HIPPO): fine-grained,
980 global-scale measurements of climatically important atmospheric gases and aerosols,
981 Philo T. R. Soc. A, 369, 2073–86, doi:10.1098/rsta.2010.0313, 2011.
982 Wu, T., Song, L., Li, W., Wang, Z., Zhang, H., Xin, X., Zhang, Y., Zhang, L., Li, J., Wu, F.,
983 Liu, Y., Zhang, F., Shi, X., Chu, M., Zhang, J., Fang, Y., Wang, F., Lu, Y., Liu, X., Wei,
984 M., Liu, Q., Zhou, W., Dong, M., Zhao, Q., Ji, J., Li, L., Zhou, M.: An overview of BCC
985 climate system model development and application for climate change studies. J. Meteor.
986 Res., 28(1), 34-56, 2014.
987 Wu, T., Li, W., Ji, J., Xin, X., Li, L., Wang, Z, Zhang, Y., Li, J., Zhang, F., Wei, M., Shi, X.,
988 Wu, F., Zhang, L., Chu, M., Jie, W., Liu, Y., Wang, F., Liu, X., Li, Q., Dong, M., Liang,

X., Gao, Y., Zhang, J.: Global carbon budgets simulated by the Beijing climate center climate system model for the last century. J Geophys Res Atmos, 118, 4326-4347. doi: 10.1002/jgrd.50320, 2013.

Wu, T., Lu, Y., Fang, Y., Xin, X., Li, L., Li, W., Jie, W., Zhang, J., Liu, Y., Zhang, L., Zhang, F., Zhang, Y., Wu, F., Li, J., Chu, M., Wang, Z., Shi, X., Liu, X., Wei, M., Huang, A., Zhang, Y., and Liu, X.: The Beijing Climate Center Climate System Model (BCC-CSM): the main progress from CMIP5 to CMIP6, Geos.Model Dev., 12, 1573-1600, http://doi/.org/10.5194/gmd-12-1573-2019, 2019.

Young, P. J., Archibald, A. T., Bowman, K. W., Lamarque, J. F., Naik, V., Stevenson, D. S., Tilmes, S., Voulgarakis, A., Wild, O., Bergmann, D., Cameron-Smith, P., Cionni, I., Collins, W. J., Dalsøren, S. B., Doherty, R. M., Eyring, V., Faluvegi, G., Horowitz, L. W., Josse, B., Lee, Y. H., MacKenzie, I. A., Nagashima, T., Plummer, D. A., Righi, M., Rumbold, S. T., Skeie, R. B., Shindell, D. T., Strode, S. A., Sudo, K., Szopa, S., and Zeng, G.: Pre-industrial to end 21st century projections of tropospheric ozone from the Atmospheric Chemistry and Climate Model Intercomparison Project (ACCMIP), Atmos. Chem. Phys., 13, 2063-2090, http://doi/.org/10.5194/acp-13-2063-2013, 2013.

Young, P. J., Naik, V., Fiore, A. M., Gaudel, A., Guo, J., Lin, M. Y., Neu, J. L., Parrish, D. D., Rieder, H. E., Schnell, J. L., Tilmes, S., Wild, O., Zhang, L., Ziemke, J. R., Brandt, J., Delcloo, A., Doherty, R. M., Geels, C., Hegglin, M. I., Hu, L., Im, U., Kumar, R., Luhar, A., Murray, L., Plummer, D., Rodriguez, J., Saiz-Lopez, A., Schultz, M. G., Woodhouse, M. T., and Zeng, G.: Tropospheric Ozone Assessment Report: Assessment of global-scale model performance for global and regional ozone distributions, variability, and trends, Elem Sci Anth, 6, 10, http://doi/.org/10.1525/elementa.265, 2018.

Zender, C., Bian, H., and Newman, D.: Mineral Dust Entrainment and Deposition (DEAD) model: Description and 1990s dust climatology, J. Geophys. Res., 108(D14), 4416, doi: 10.1029/2002JD002775, 2003.

Table 1. Chemical species considered in BCC-AGCM3-Chem. Species marked with star (*) denote those added in BCC-ESM1 apart from the 63 species used in MOZART2. In the column of surface emission, interactive surface emissions are considered for sea salt and dust.

Species		Dry deposition	Wet deposition	Surface emission	Aircraft emission	Volcanic emission
Gas tracers	O_3	√				
	N_2O			√		
	N					
	NO	√		√	√	
	NO_2	√				
	NO_3					
	HNO_3	√	√			
	HO_2NO_2	√	√			
	N_2O_5					
	CH_4	√		√	√	
	CH_3O_2					
	CH_3OOH	√	√			
	CH_2O	√	√	√		
	CO	√		√	√	
	OH					
	HO_2					
	H_2O_2	√	√			
	C_3H_6			√		
	ISOP			√		
	PO_2					
	CH_3CHO	√	√	√		
	POOH	√	√			
	CH_3CO_3					
	CH_3COOOH	√	√			
	PAN	√				
	ONIT	√	√			
	C_2H_6			√		
	C_2H_4			√		
	C_4H_{10}			√		
	MPAN	√				
	$ISOPO_2$					
	MVK		√			
	MACR		√			
	$MACRO_2$					
	MACROOH	√	√			
	MCO_3					
	$C_2H_5O_2$					
	C_2H_5OOH	√	√			
	$C_{10}H_{16}$			√		

1022 Table 1. Continued.

Species name		Dry deposition	Wet deposition	Surface emission	Aircraft emission	Volcanic emission
Gas tracers	C_3H_8			√		
	$C_3H_7O_2$					
	C_3H_7OOH	√	√			
	CH_3COCH_3	√		√		
	ROOH		√			
	CH_3OH	√	√	√		
	C_2H_5OH	√	√	√		
	GLYALD	√	√			
	HYAC	√	√			
	EO_2					
	EO					
	HYDRALD	√	√			
	RO_2					
	CH_3COCHO	√	√	√		
	Rn-222					
	Pb-210	√	√			
	$ISOPNO_3$		√			
	ONITR	√	√			
	XO_2					
	XOOH	√	√			
	ISOPOOH	√	√			
	H_2	√		√		
	Stratospheric O_3	√				
	Inert O_3	√				
	SO_2*	√	√	√	√	√
	DMS*			√		
	NH_3*			√	√	
Aerosols	SO_4^{2-}*	√	√			
	OC1*	√	√	√	√	
	OC2*	√	√	√	√	
	BC1*	√	√	√	√	
	BC2*	√	√	√	√	
	SSLT01*	√	√			
	SSLT02*	√	√			
	SSLT03*	√	√			
	SSLT04*	√	√			
	DST01*	√	√			
	DST02*	√	√			
	DST03*	√	√			
	DST04*	√	√			

1023

1024

1025 Table 2. Gas-phase chemical reactions for NH_3 and bulk aerosols precursors following
1026 CAM-Chem (Lamarque et al., 2012). The reaction rates (s^{-1}) refer to Tie et al. (2001) and
1027 Sander et al. (2003), and Cooke and Wilson (1996). Temperature (T) is expressed in K, air
1028 density (M) in molecule cm^{-3}, ki and ko in cm^3 molecule^{-1} s^{-1}.
1029

Chemical reactions	Rate
NH_3+ OH → H_2O	1.70E-12*exp(–710/T)
SO_2 + OH → SO_4^{2-}	ko/(1.+ko*M/ki)*f**(1./(1.+log10(ko*M/ki)), in which ko=3.0E-31*(300/T)**3.3; ki=1.E-12; f =0.6
DMS + OH → SO_2	9.60E-12*exp(-234./T)
DMS + OH → .5*SO_2 + .5*HO_2	1.7E−42*exp(7810/T)*M*0.21/(1+5.5E−31*exp(7460/T)* M* 0.21)
DMS + NO_3 → SO_2 + HNO_3	1.90E-13*exp(520/T)
BC1 → BC2	7.10E-06
OC1 → OC2	7.10E-06

1030
1031

Table 3. Size and density parameters of bulk aerosols.

Aerosols	Species Name	Mean radius (μm) / bin size (μm)	Geometric standard deviation (μm)	Density (g cm^{-3})
SO_4^{2-}	Sulfate	0.05	2.03	1.77
BC1	hydrophobic black carbon	0.02	2.00	1.0
BC2	hydrophilic black carbon	0.02	2.00	1.0
OC1	hydrophobic organic carbon	0.03	2.24	1.8
OC2	hydrophilic organic carbon	0.03	2.24	1.8
DST01	Dust	0.55/ bin: 0.1-1.0	2.00	2.5
DST02	Dust	1.75 / bin: 1.0-2.5	2.00	2.5
DST03	Dust	3.75 / bin: 2.5-5.0	2.00	2.5
DST04	Dust	7.50 / bin: 5.0-10.	2.00	2.5
SSLT01	Sea salt	0.52 / bin: 0.2-1.0	2.00	2.2
SSLT02	Sea salt	2.38 / bin: 1.0-3.0	2.00	2.2
SSLT03	Sea salt	4.86 / bin: 3.0-10.	2.00	2.2
SSLT04	Sea salt	15.14 / bin: 10.-20.	2.00	2.2

Table 4. Source of emission data. MOZART2 data denote the standard tropospheric chemistry package for MOZART contains surface emissions from the EDGAR 2.0 data base (Olivier et al., 1996). ACCMIP data are downloaded from the IPCC ACCMIP emission inventory (http://accent.aero.jussieu.fr/ACCMIP.php) and they vary from 1850 to 2000, in 10-year steps (Lamarque et al., 2010). CMIP6 data are from https://esgf-node.llnl.gov/search/input4mips/. Anthropogenic emission includes Industrial and fossil fuel use, agriculture, ships, and etc. Biomass burning includes vegetation fires incl. fuel wood and agricultural burning.

Species	Anthropogenic emission	Biomass burning	Biogenic emissions from vegetation	Biogenic emissions from soil	Oceanic emissions	Airplane emission	Volcanic emission
C_2H_4	CMIP6	CMIP6	On-line computation		MOZART2		
C_2H_5OH	CMIP6	CMIP6					
C_2H_6	CMIP6	CMIP6	ACCMIP		MOZART2		
C_3H_6	CMIP6	CMIP6	On-line computation		MOZART2		
C_3H_8	CMIP6	CMIP6	ACCMIP		MOZART2		
C_4H_{10}	CMIP6	CMIP5	MOZART2		MOZART2		
CH_2O	CMIP6	CMIP6					
CH_3CHO	ACCMIP	CMIP6					
CH_3COCHO		CMIP6					
CH_3OH	ACCMIP	CMIP6	ACCMIP				
CH_3COCH_3	ACCMIP	ACCMIP	On-line computation		MOZART2		
ISOP		CMIP5	On-line computation				
$C_{10}H_{16}$		CMIP6	On-line computation				
CH_4	CMIP6	CMIP6	MOZART2		MOZART2	CMIP6	
CO	CMIP6	CMIP6	ACCMIP	MOZART2	ACCMIP	CMIP6	
H_2	MOZART2	CMIP6		MOZART2	MOZART2		
N_2O	MOZART2	CMIP6		MOZART2	MOZART2		
NH_3	CMIP6	CMIP6		ACCMIP	ACCMIP	CMIP6	
NO	CMIP6	CMIP6		ACCMIP		CMIP6	
SO_2	CMIP6	CMIP6				CMIP6	ACCMIP
DMS					ACCMIP		
OC1	CMIP6	CMIP6				CMIP6	
OC2	CMIP6	CMIP6	On-line computation			CMIP6	
BC1	CMIP6	CMIP6				CMIP6	
BC2	CMIP6	CMIP6				CMIP6	

Table 5. Global budgets for DMS, SO_2, and sulfate in the period of 1991 to 2000. Units are sources and sinks, Tg(S) yr^{-1}; burden, Tg; lifetime, days.

		BCC-ESM (1991-2000 mean)	Other studies and CMIP5 data
DMS	Sources	27.4	
	Emission	27.4	10.7-23.7[a]
	Sinks	28.0	
	Gas-phase oxidation	28.0	
	Burden	0.12	0.04-0.29[a]
	Lifetime	0.78	0.5-3.0[a]
SO_2	Sources	76.93	
	Emission at surface	63.63	
	Emission from airplane	0.10	
	DMS oxidation	13.20	10.0-24.7[a]
	Sinks	76.96	
	Dry deposition	18.53	16.0-55.0[a]
	Wet deposition	9.36	0.0-19.9[a]
	Gas-phase oxidation	10.33	6.1-16.8[a]
	Aqueous-phase oxidation	38.74	24.5-57.8[a]
	Burden	0.48	0.40-1.22[a]
	Lifetime	1.12	0.6-2.6[a]
SO_4^{2-}	Sources	49.05	59.67±13.13[b]
	Emission	0.00	
	SO_2 aqueous-phase oxidation	38.73	
	SO_2 gas-phase oxidation	10.32	
	Sinks	49.06	
	Dry deposition	2.20	4.96-5.51[d]
	Wet deposition	46.86	39.34-40.20[d]
	Burden	1.89	1.98±0.48[b], 1.71[c],1.2[g], 2.22-2.43[h]
	Lifetime	4.69	4.12±0.74[b], 3.72-3.77[d] 3.3[g], 3.7-4.0[h]

Notes: References denote a for Liu et al. (2005), b for Textor et al. (2006), c for the values derived from CMIP5 prescribed aerosol masses averaged from 1991 to 2000, d for Liu et al. (2012), g for Matsui and Mahowald (2017), and h for Tegen et al. (2019). Values of DMS, SO_2, and sulfate burdens in the literature d are transferred from TgS to Tg (species) for units consistence.

Table 6. Same as Table 5, but for global budgets for black carbon, organic carbon, dust, and sea salts. Units are sources and sinks, Tg yr^{-1}; burden, Tg; lifetime, days.

		BCC-ESM (1991-2000 mean)	Other studies and CMIP5 data
BC	Sources	7.22	
	Emission	7.22	11.9±2.7[b], 7.8[g]
	Sinks	7.24	7.75[d], 7.8[g]
	Dry deposition	0.90	0.27[g], 1.30-1.64[e]
	Wet deposition	6.34	7.5[g], 6.10-6.45[e]
	Burden	0.13	0.114[c], 0.24±0.1[b], 0.11[g],0.14-0.26[h], 0.084-0.123[e]
	Lifetime	6.60	7.12±2.35[b], 3.95-4.80[e], 5.0[g], 6.3-7.5[h]
OC	Sources	32.29	
	Fossil and biofuel emission	13.91	
	Natural emission	18.38	
	Sinks	32.30	
	Dry deposition	2.44	
	Wet deposition	29.86	
	Burden	0.62	0.69[c], 1.7±0.45[b],1.0-2.2[h]
	Lifetime	5.00	6.54±1.76[b], 4.56−4.90[d], 6.4[g],5.4-6.6[h]
Dust	Sources	2592.0	1840[b],2943.5−3121.9[d], 2677[g]
	Sinks	2592.0	
	Dry deposition	1630.8	1444[g]
	Wet deposition	961.2	1245[g]
	Burden	22.93	20.41[c], 22.424.7[d], 35.9[f], 19.2±7.68[b], 28.5[g], 16.5-17.9[h]
	Lifetime	3.23	4.14±1.78[b], 2.61−3.07[d], 3.9[g], 5.3-5.7[h]
Sea Salt	Sources	4667.2	4965.5-5004.1[d], 5039[g]
	Sinks	4667.4	
	Dry deposition	2978.5	2158[g]
	Wet deposition	1688.9	2918[g]
	Burden	11.89	7.58−10.37[a], 6.4±3.4[b], 11.84[c], 13.6[g], 3.9[h]
	Lifetime	0.93	0.41±0.24[b],0.55−0.76[d], 0.98[g], 1.2-1.3[h]

Notes: References denote a for Liu et al. (2005), b for Textor et al. (2006), c derived from CMIP5 prescribed aerosol masses averaged from 1991 to 2000, d for Liu et al. (2012), e for Liu et al. (2016), f for Ginoux (2001), g for Matsui and Mahowald (2017), and h for Tegen et al. (2019).

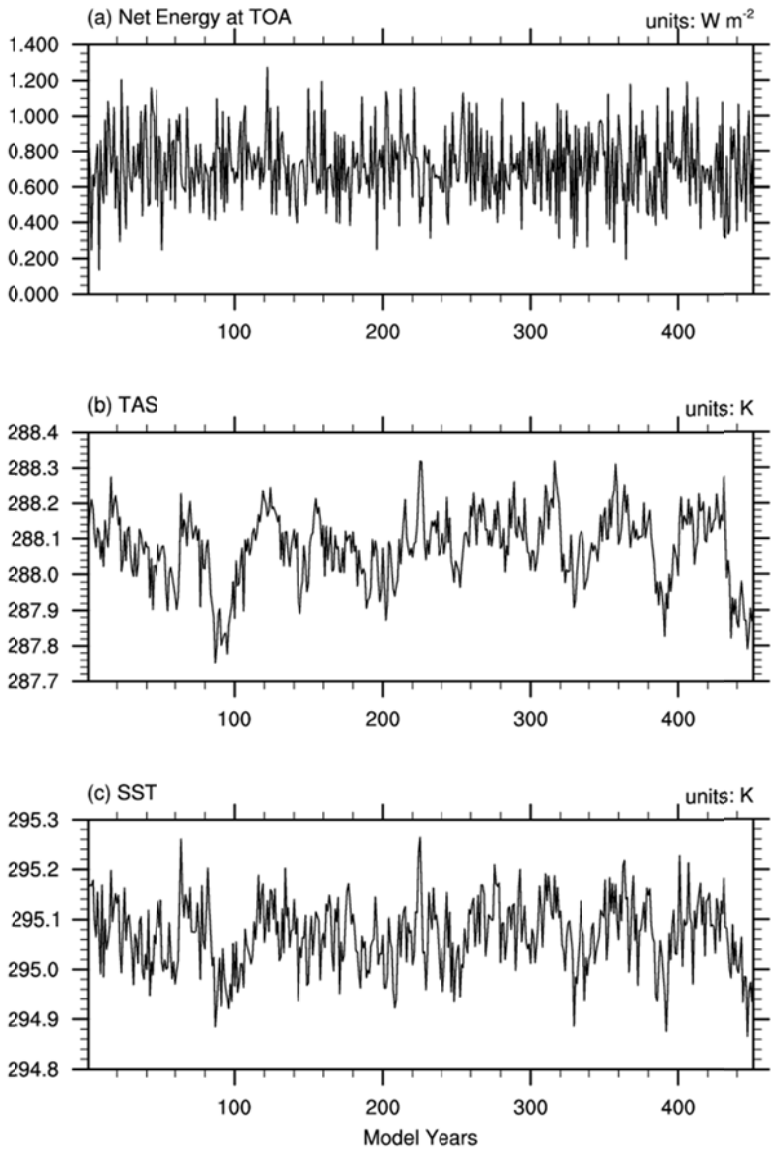

Figure 1. The time series of global and annual mean of (a) net energy budget at top of atmosphere ($W \cdot m^{-2}$), (b) near-surface air temperature (K), and (c) sea surface temperature (K) in the last 450 years of the piControl simulation.

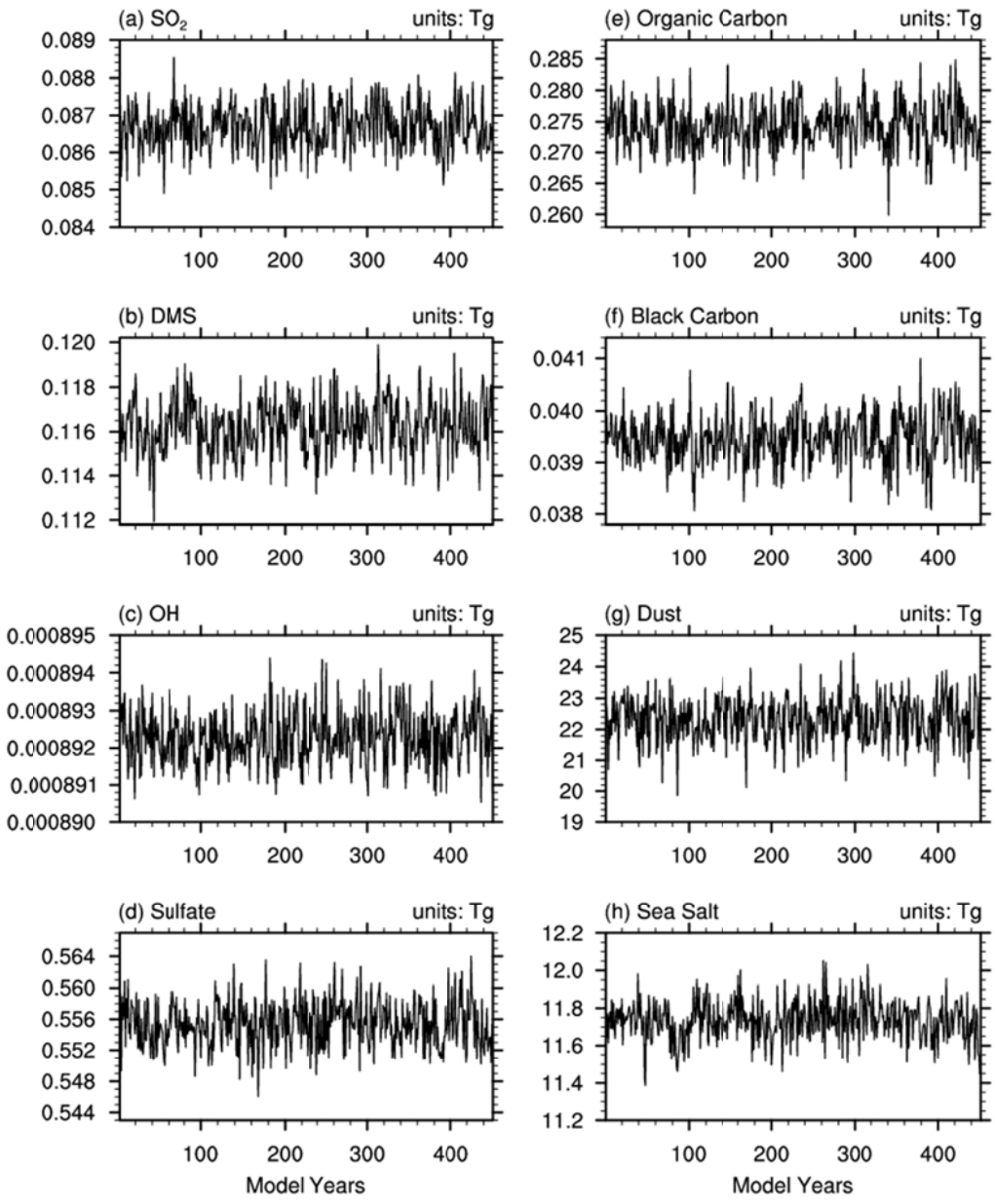

Figure 2. Same as in Figure 1, but for the global burdens of (a) SO_2, (b) DMS, (c) OH, and (d-h) different aerosols in the troposphere (below 100 hPa). Units are Tg.

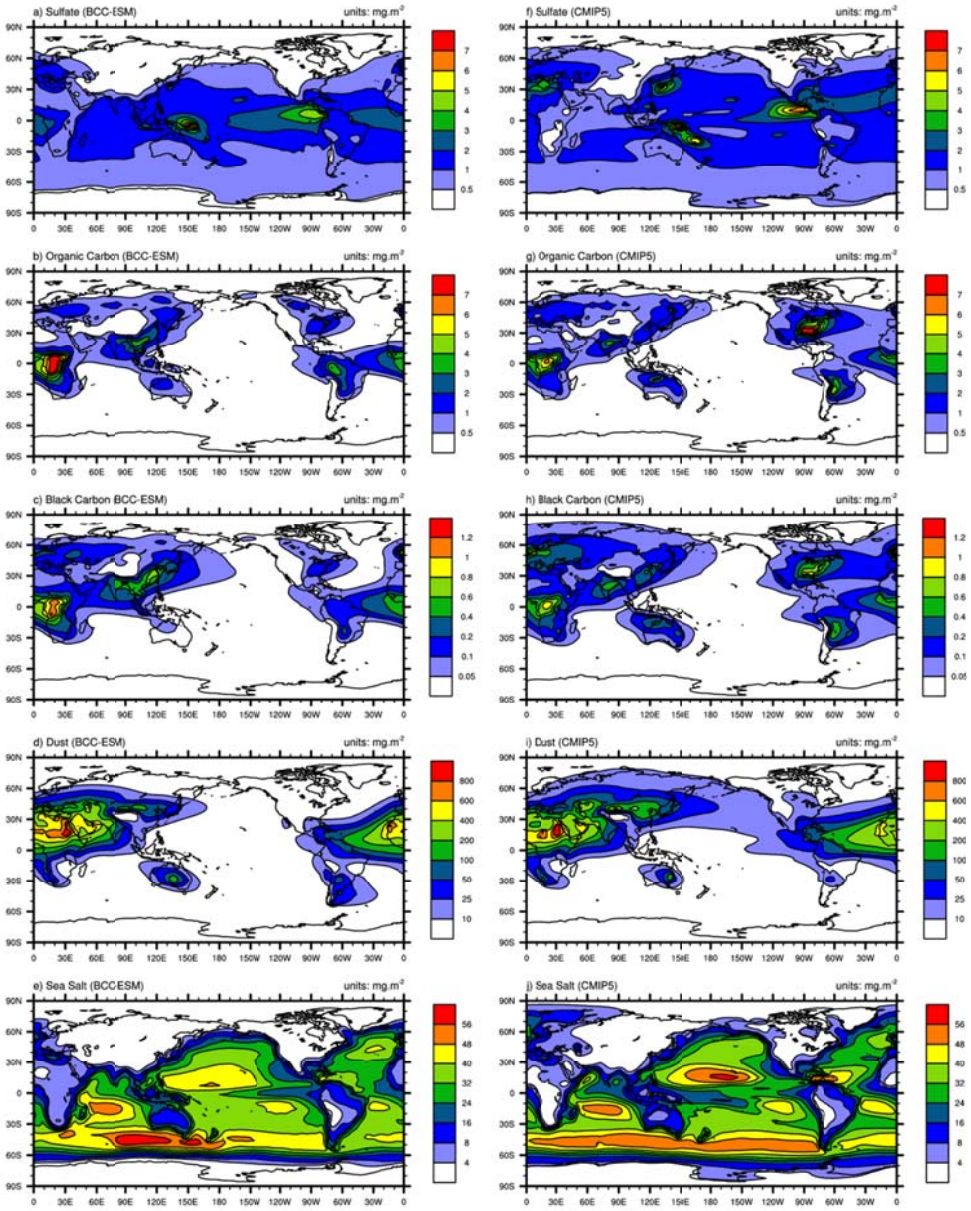

Figure 3. Global distributions of annual mean mass burdens of sulfate (SO_4^{2-}; first row), organic carbon (OC; second row), black carbon (BC; third row), dust (fourth row), and sea salt (fifth row) aerosols in the whole atmospheric column. The left panels show the mean averaged for the last 100 years of BCC-ESM pre-industrial piControl simulations, and the right panels show the CMIP5 recommended aerosol concentrations in year 1850 (the website at IIASA http://tntcat.iiasa.ac.at/RcpDb/.). Units: $mg \cdot m^{-2}$.

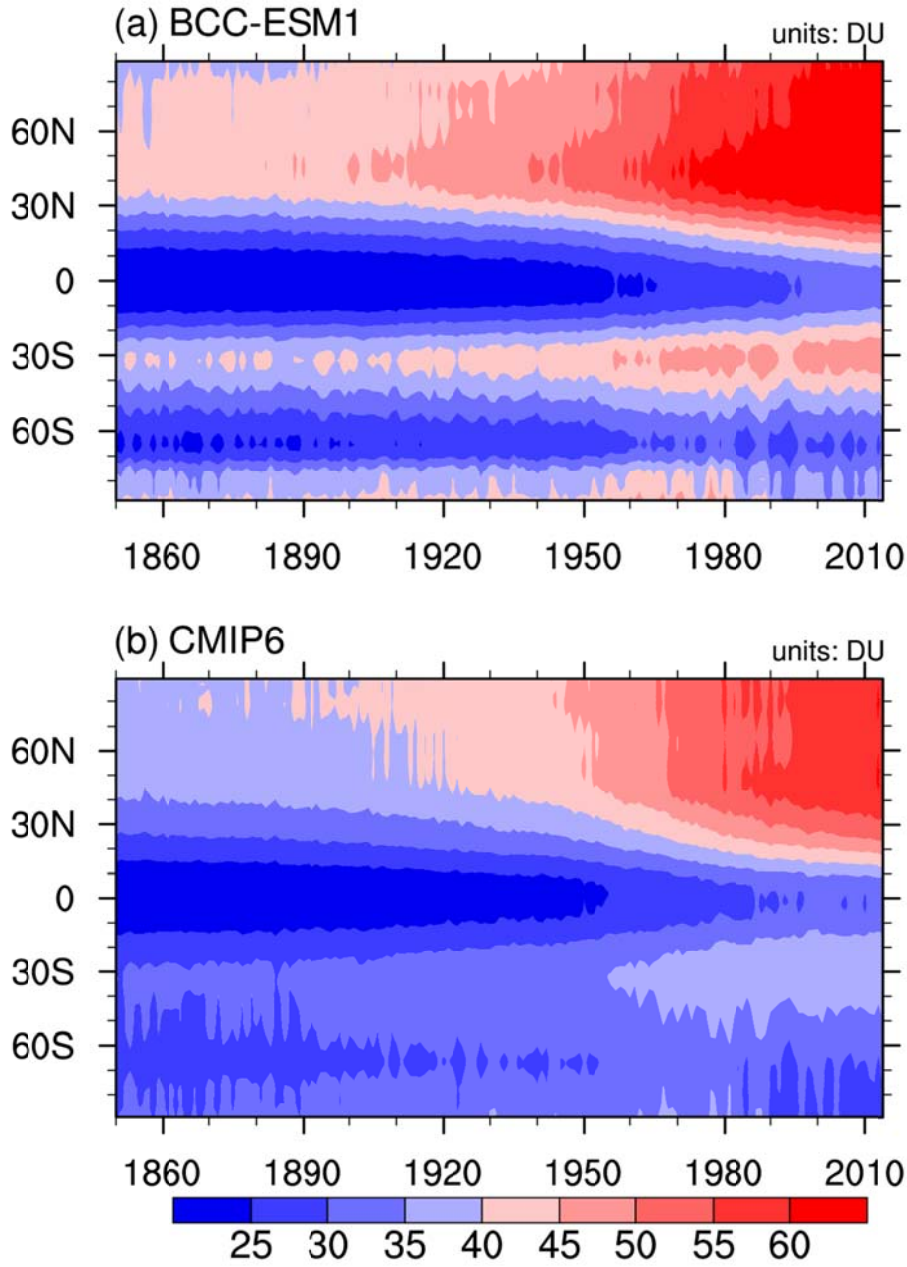

Figure 4. Zonal mean of yearly mean concentration of ozone column in the troposphere below 300 hPa to the ground from 1871 to 1999 for (a) BCC-ESM1 and (b) CMIP6 data. Unit: DU.

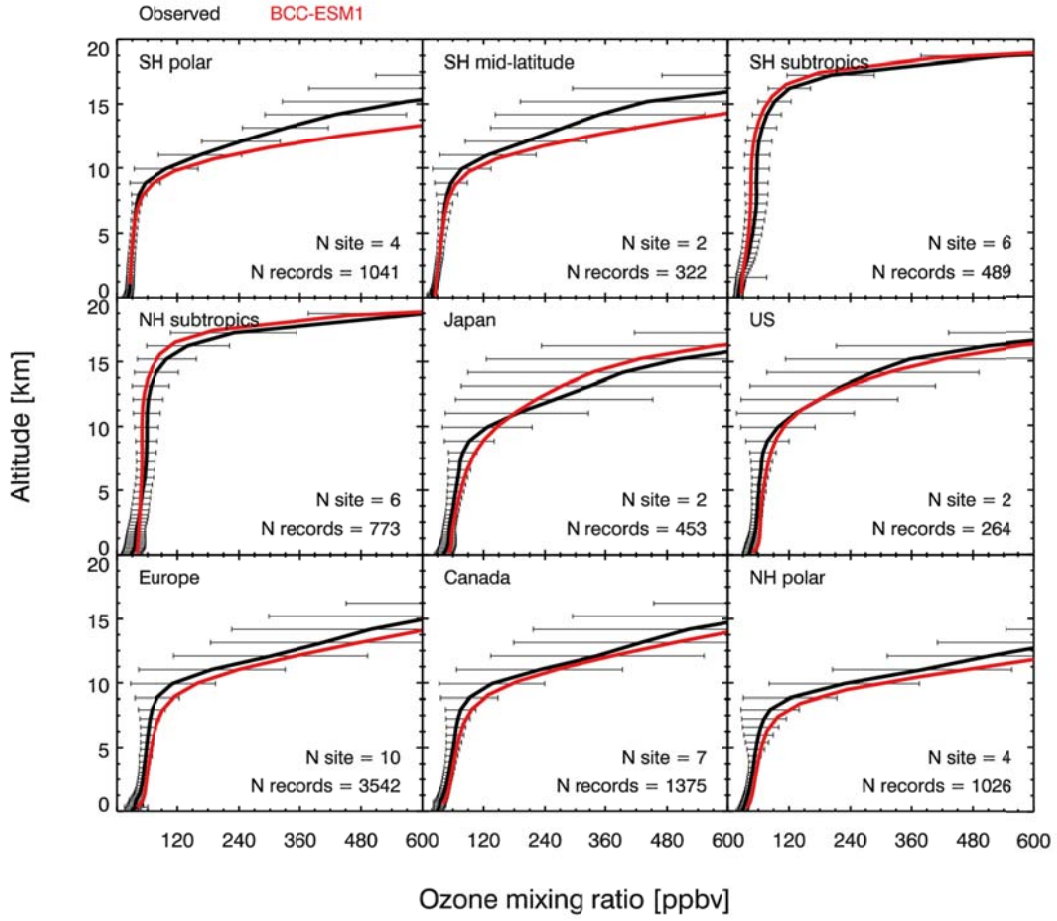

Figure 5. Vertical profiles of annual mean ozone concentrations from observations averaged for 2010-2014 in nine regions (black) and from the BCC-ESM1 simulations (red). The observations are derived from 41 global WOUDC sites.

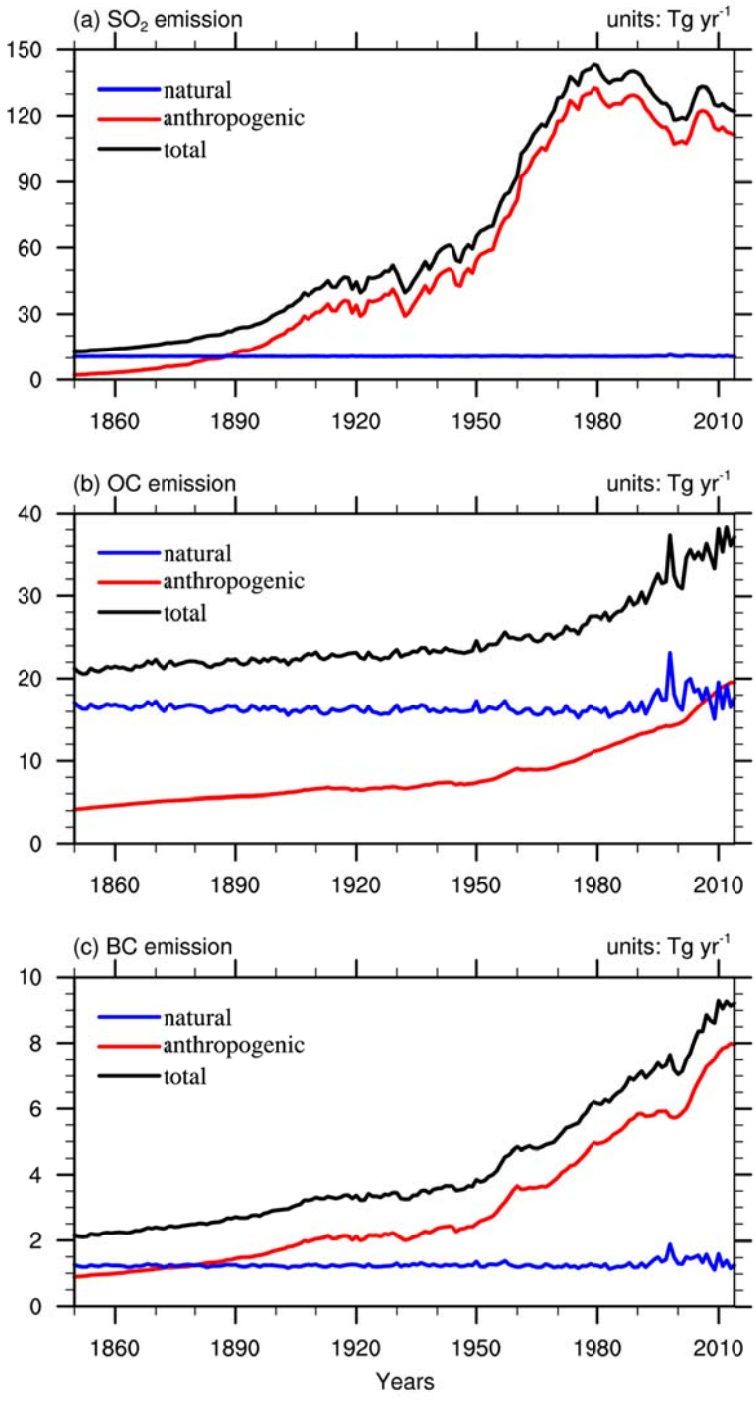

Figure 6. Global annual anthropogenic, natural, and total emissions of SO_2, organic carbon (OC), and black carbon (BC) in the BCC-ESM1 historical simulation. All the biomass burning emissions are included in natural emissions in (a)-(c). Units: Tg yr^{-1}.

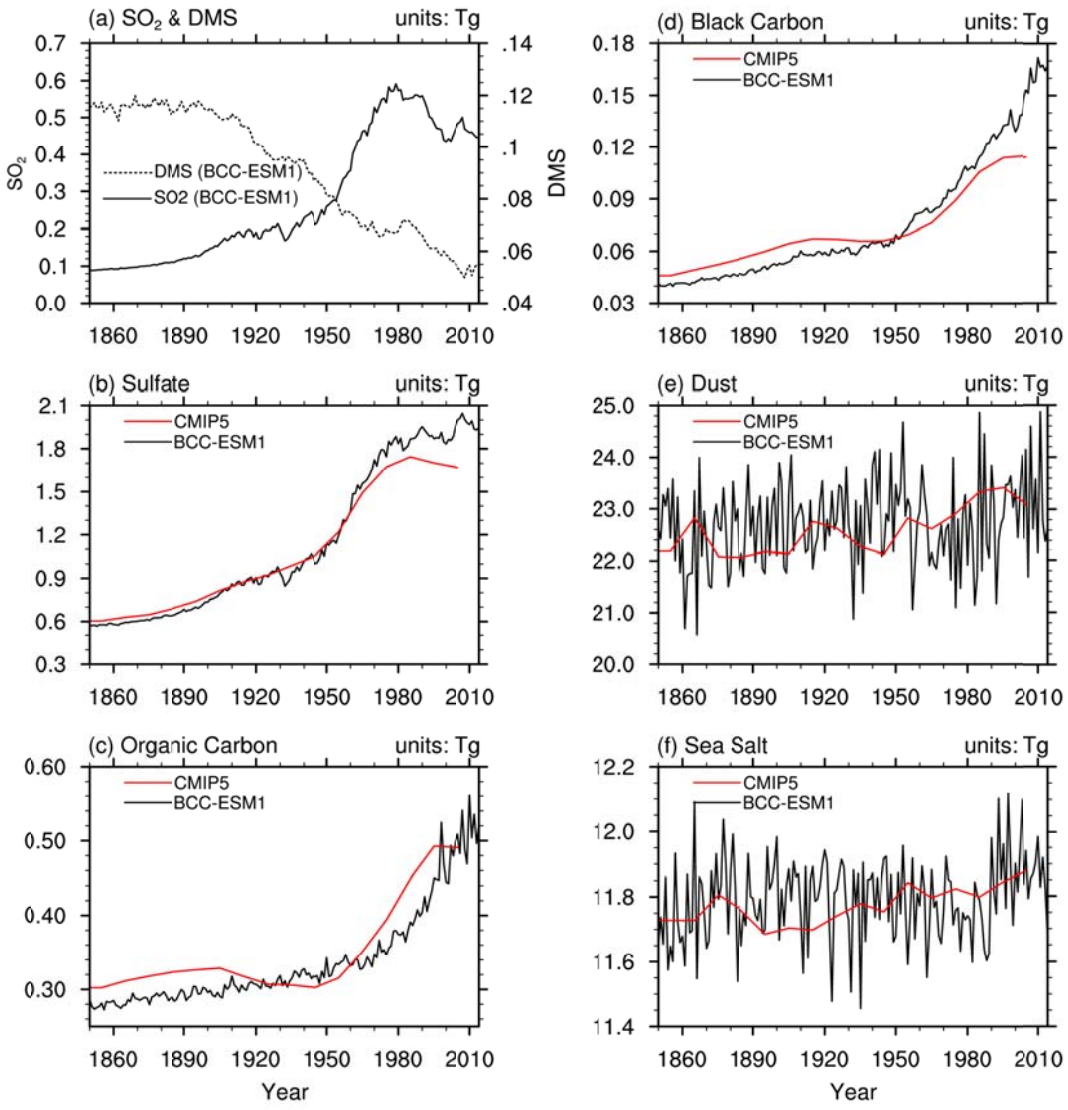

Figure 7. The time series of global yearly amounts of (a) SO_2 and DMS and (b-f) aerosols in the whole atmosphere column from the CMIP6 historical simulations of BCC-ESM1 (black lines) and the CMIP5-recommended aerosols masses (red lines). The yearly CMIP5 data are interpolated from the time series in 10-year interval. Units: Tg.

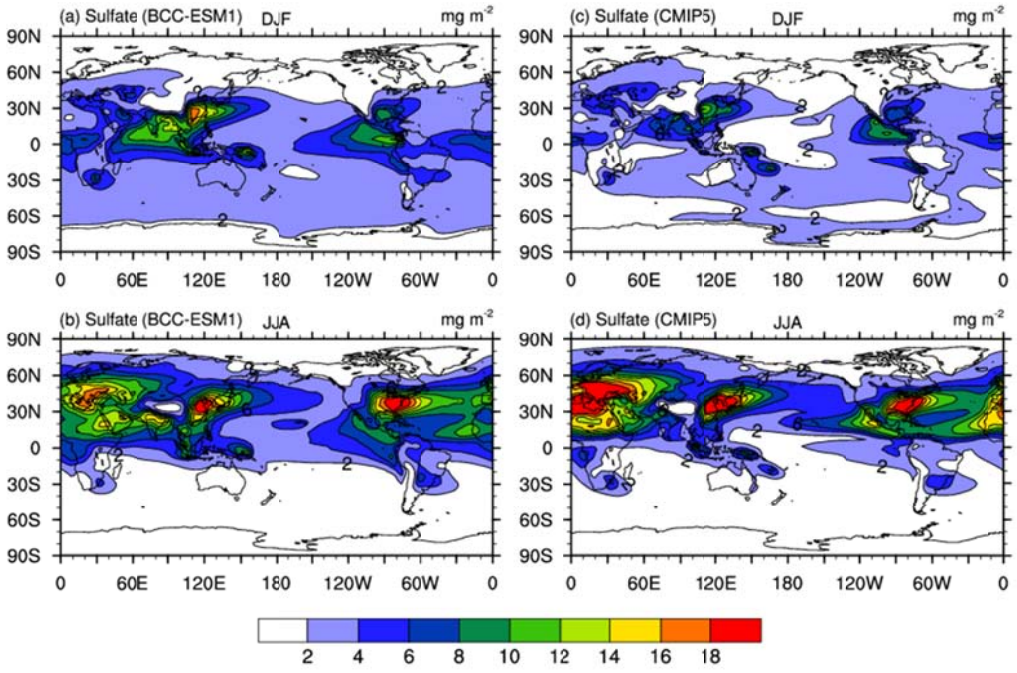

Figure 8. December-January-February (DJF; top panels) and June-July-August (JJA; bottom panels) mean sulfate (SO_4^{2-}) aerosol column mass concentrations averaged for the period of 1971-2000. Left panels show the historical simulations of BCC-ESM1, and right panels the CMIP5-recommended data. Units: $mg.m^{-2}$.

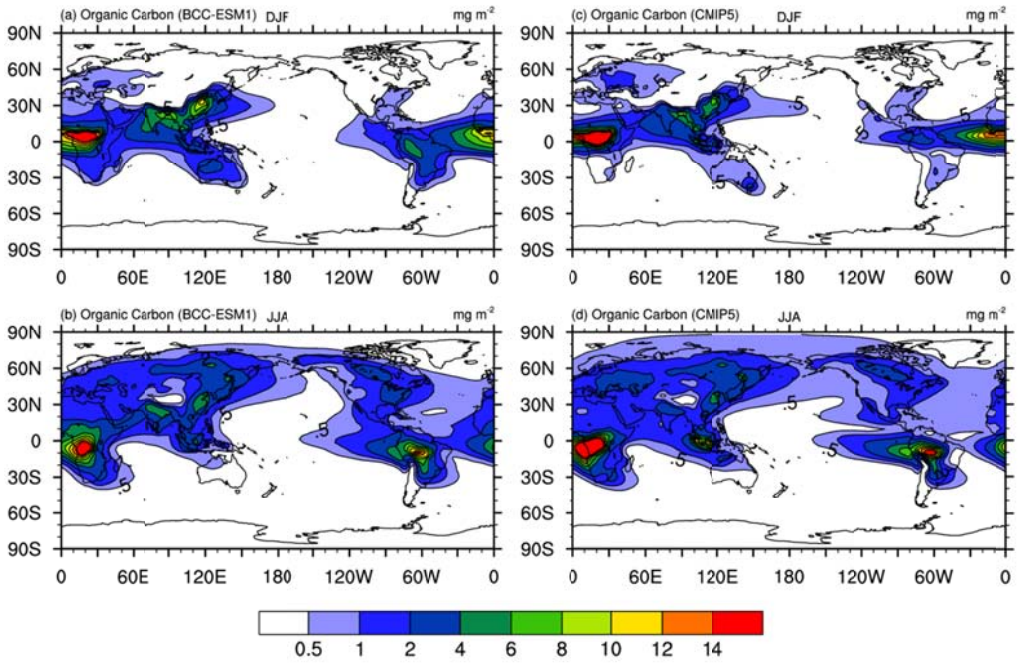

Figure 9. The same as in Figure 8, but for organic carbon (OC) aerosol column mass concentrations. Units: mg m^{-2}.

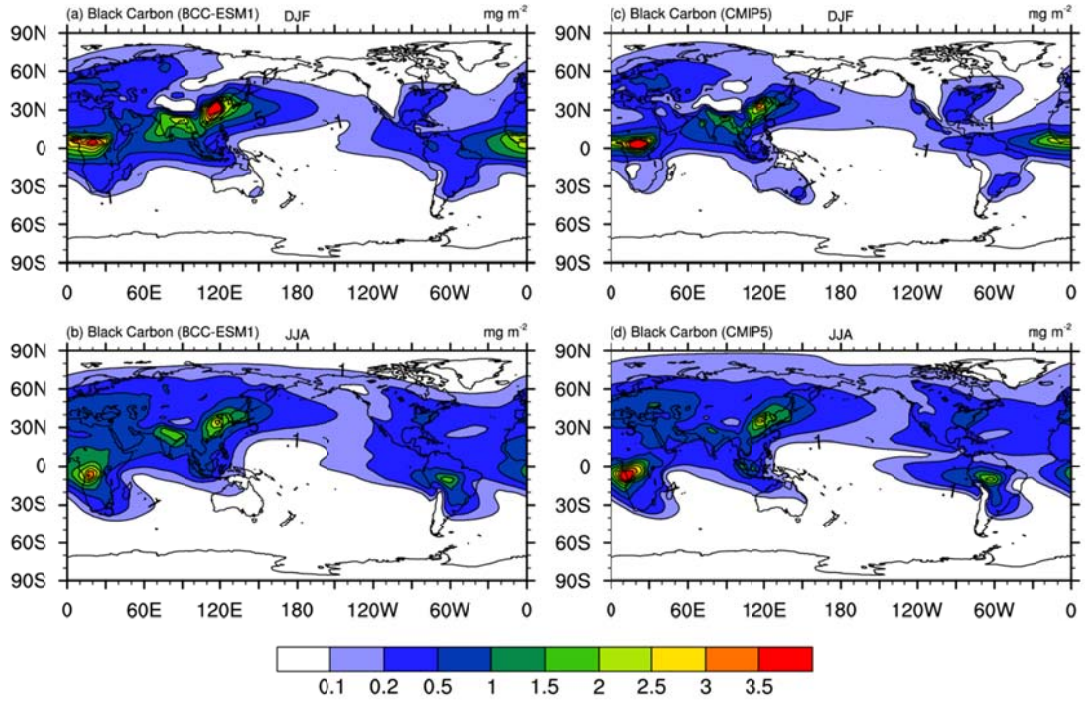

Figure 10. The same as in Figure 8, but for black carbon (BC) aerosol. Units: $mg.m^{-2}$.

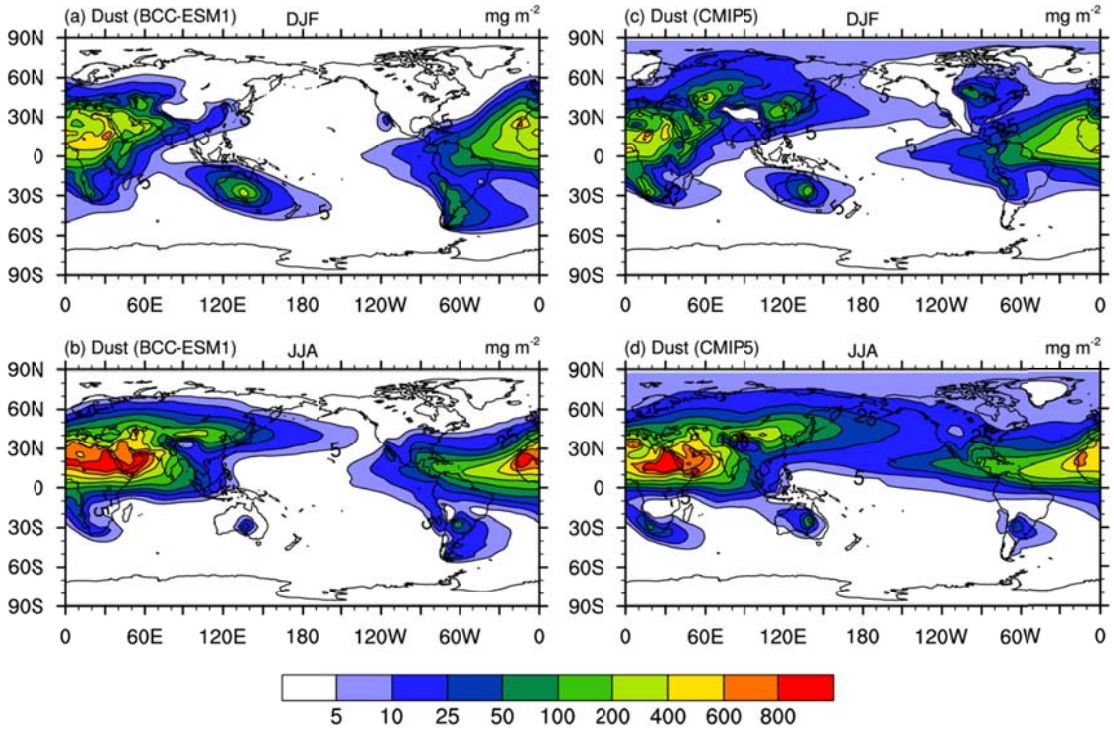

Figure 11. The same as in Figure 8, but for dust aerosol. Units: $mg.m^{-2}$.

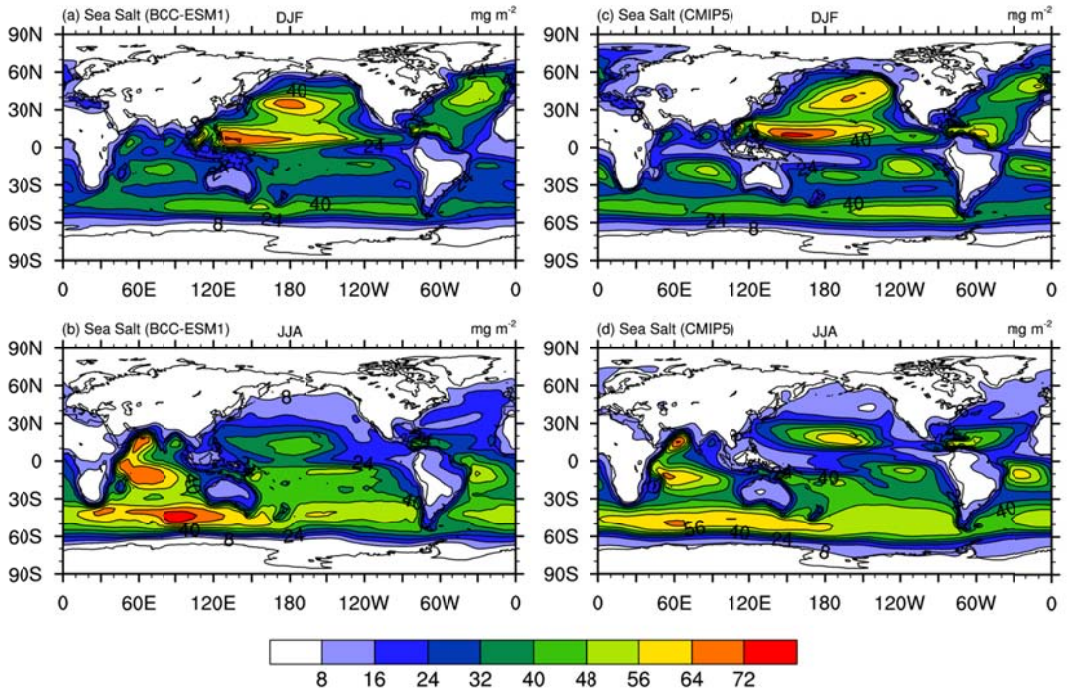

Figure 12. The same as in Figure 8, but for sea salt (SSLT) aerosol. Units: $mg.m^{-2}$.

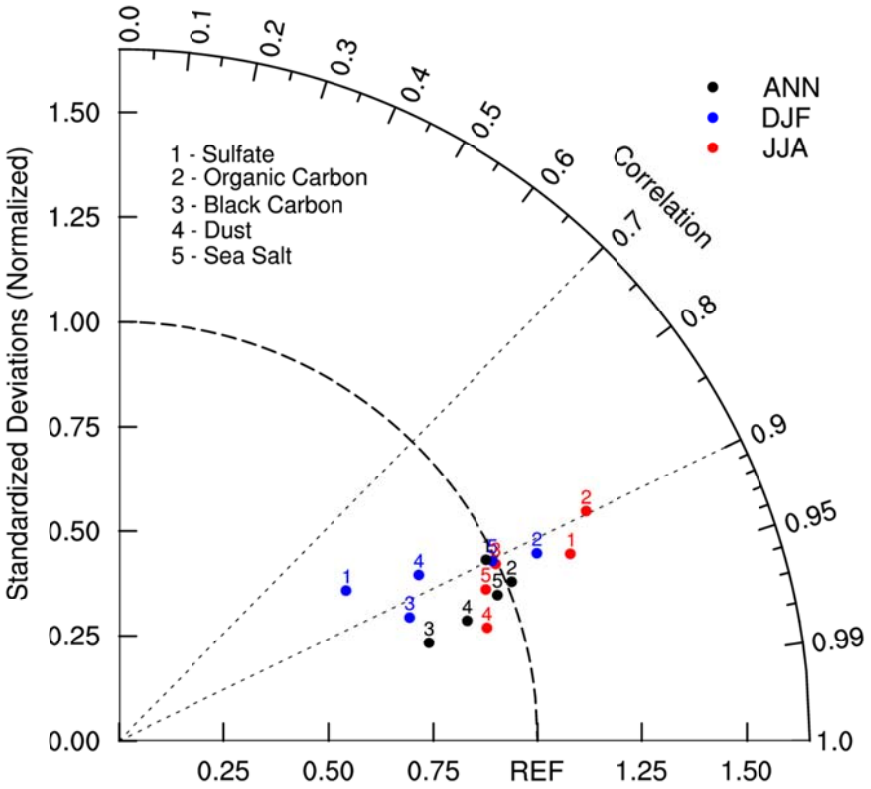

Figure 13. Taylor diagram for the global aerosols climatology (1971–2000) of sulfate, organic carbon, black carbon, dust, and sea salt averaged for December-January-February (DJF), June-July-August (JJA), and annual respectively. The radial coordinate shows the standard deviation of the spatial pattern, normalized by the observed standard deviation. The azimuthal variable shows the correlation of the modelled spatial pattern with the observed spatial pattern. Analysis is for the whole globe. The reference dataset is CMIP5-prescribed dataset.

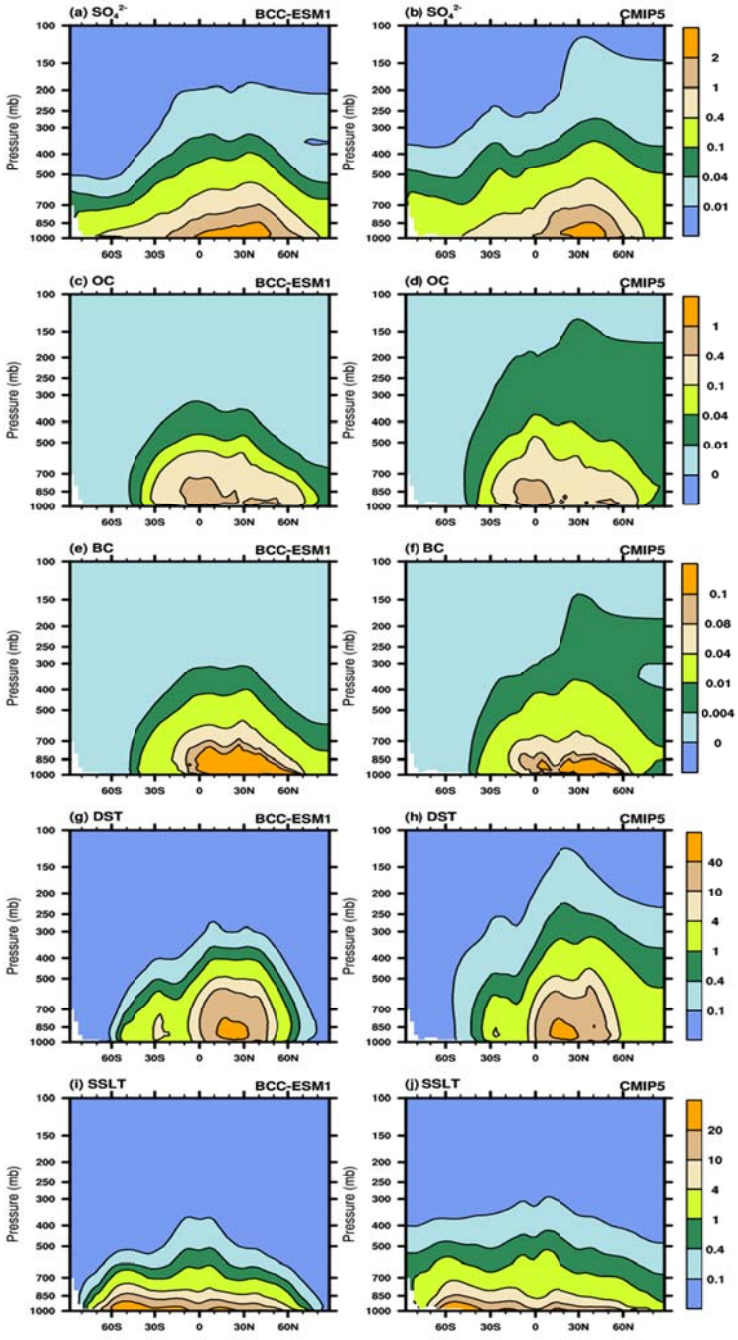

Figure 14. Latitude-pressure distributions of zonally-averaged annual mean sulfate, organic carbon, black carbon, dust, and sea salt aerosol concentrations for the period of 1971-2000. Left panels show the CMIP6 historical simulation of BCC-ESM1, and right panels the CMIP5 recommendation data. Units: μg m^{-3}.

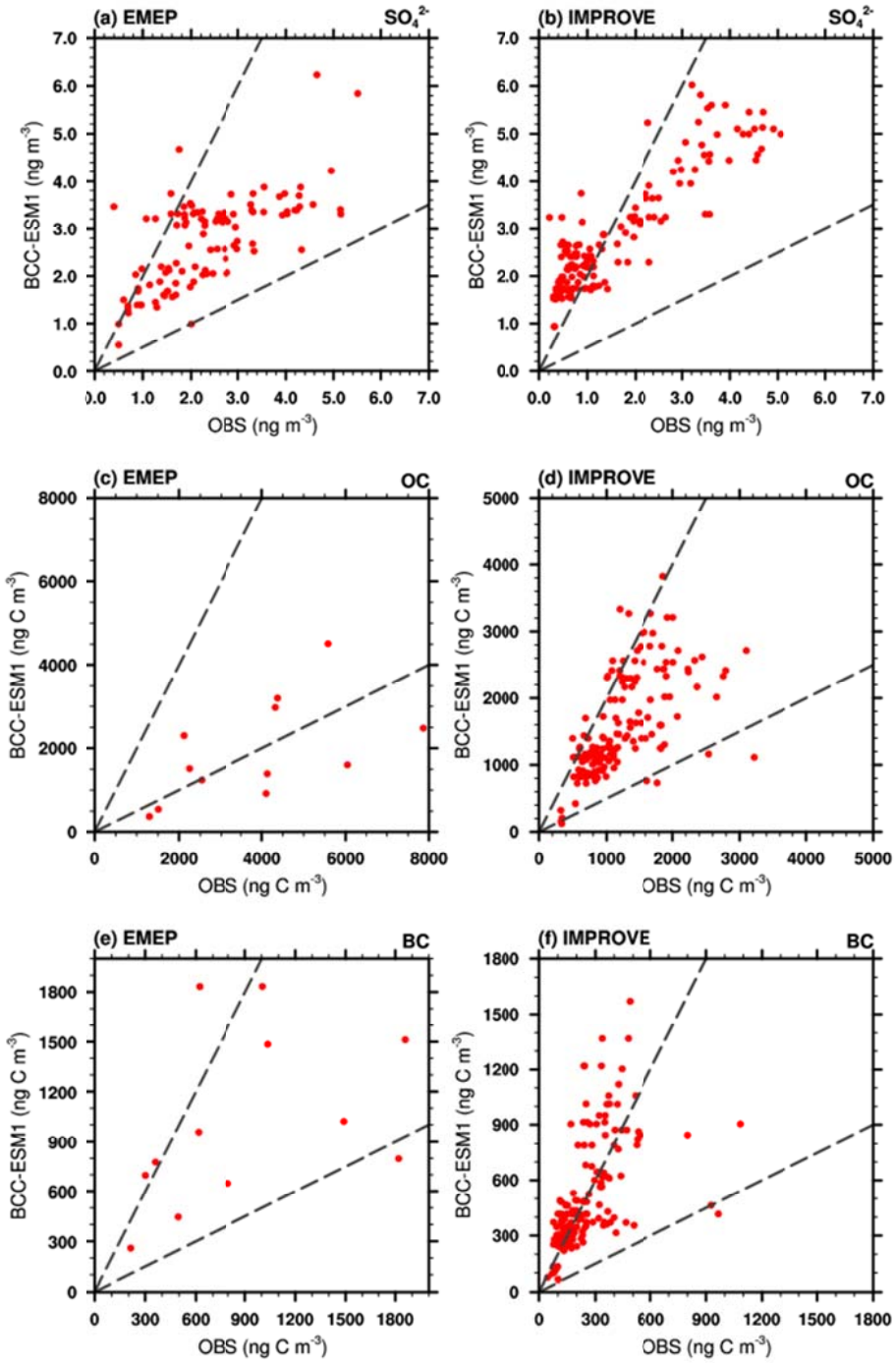

Figure 15. Scatter plots showing observed versus simulated multi-years averaged annual mean sulfate (SO_4^{2-}), organic carbon (OC), black carbon (BC) mixing ratios at IMPROVE and EMEP network sites. Observations are averages over the available years 1990–2005 for IMPROVE sites, and 1995–2005 for EMEP sites. Simulated values are those at the lowest layer of BCC-ESM1.

Table 7. Observed versus simulated concentrations of sulfate (SO_4^{2-}), organic carbon (OC), black carbon (BC) for the regional mean and spatial standard deviation, minimum and maximum values at IMPROVE and EMEP network sites, and the spatial correlation between observed and simulated multi-years averaged annual means. Simulated values are selected for the same locations and same valid observation time. The data used same as those in Figure 12.

	EMEP			**IMPROVE**		
	$SO4^{2-}$ (Obs/Model)	**OC (OBS/Model)**	**BC (OBS/Model)**	**$SO4^{2-}$ (OBS/Model)**	**OC (OBS/Model)**	**BC (OBS/Model)**
Mean Values	2.37/2.74	3844/1919	884/1022	1.53/2.79	1215/1565	249/504
Std Deviation	1.16/0.93	1997/1215	572/526	1.30/1.20	572/745	164/296
Min Values	0.40/0.55	1296/369	214/259	0.22/0.94	322/123	45/66
Max Values	5.50/6.24	7867/4510	1859/1834	5.07/6.02	3219/3827	1084/1570
Correlation (Obs and Model)	0.67	0.56	0.40	0.90	0.63	0.55

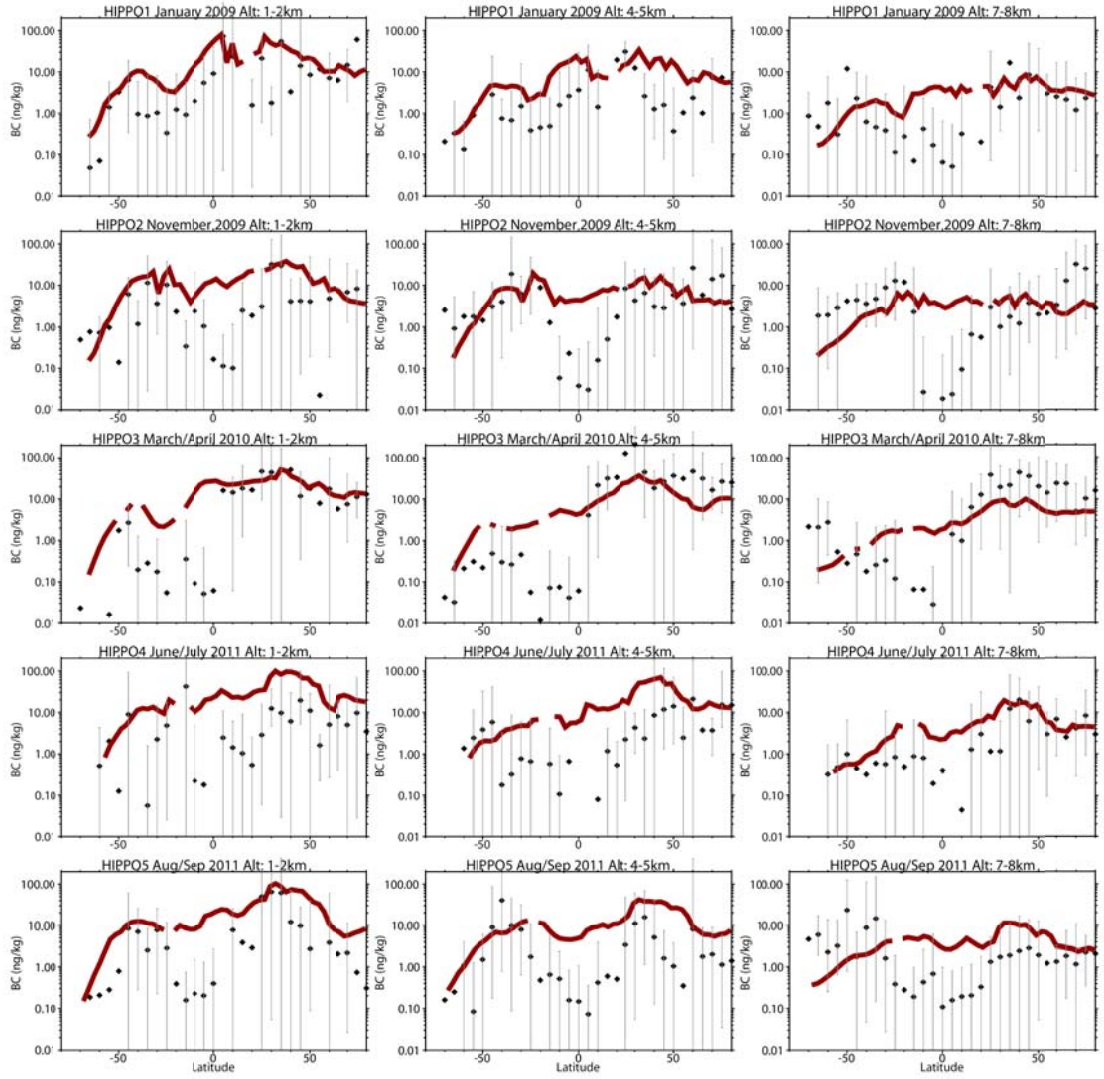

Figure 16. Comparison of modelled black carbon (BC) aerosol (red lines) with observations from HIPPO aircraft campaigns over the Pacific Ocean (black symbols, bars represent the full data range). Observations from different HIPPO campaigns were averaged over 5° latitude bins and three different altitude bands (left column: 1-2 km, middle column: 4-5 km, and right column: 7-8 km) along the flight track over the Pacific Ocean. Model results were sampled along the flight track and then averaged over the abovementioned regions for comparison.

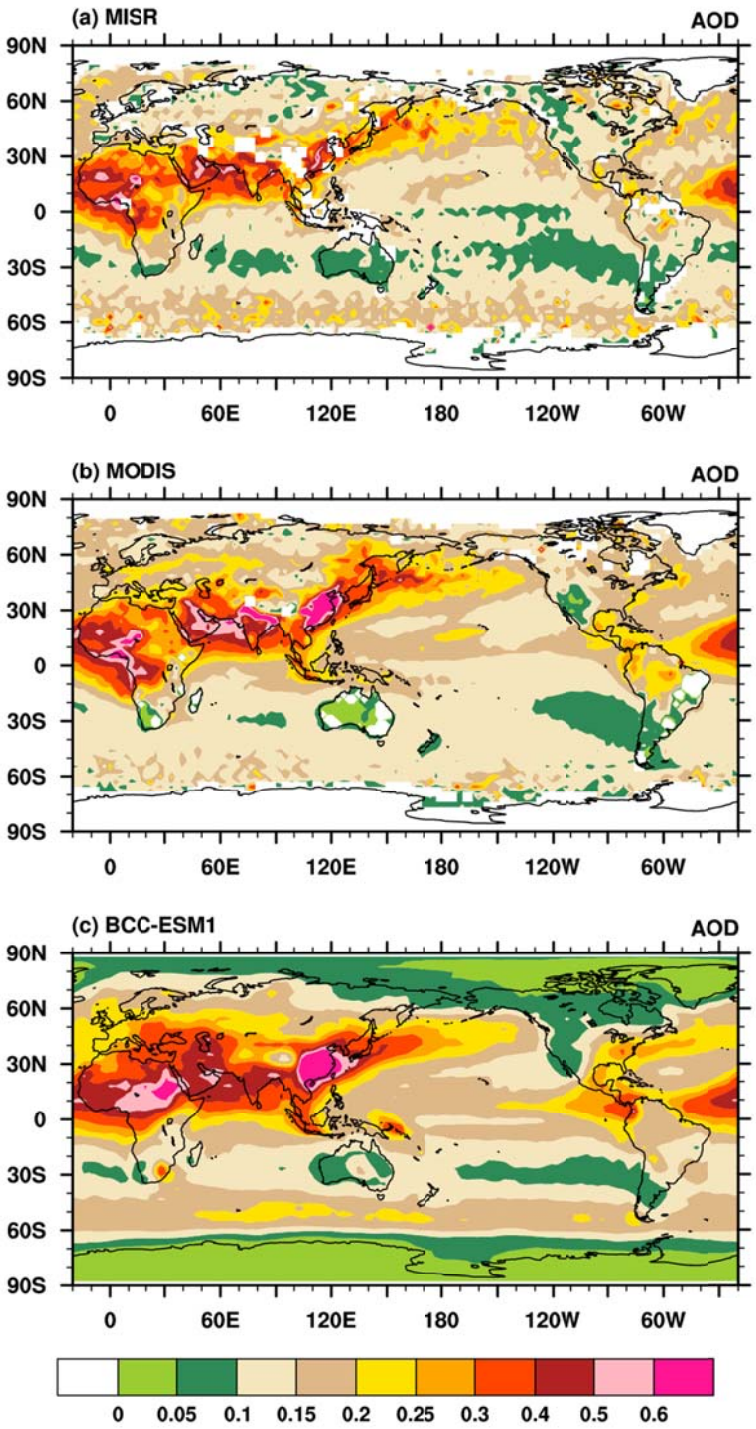

Figure 17. Global distribution of annual mean AOD simulated in BCC-ESM1 compared with the MISR and MODIS data for the year 2008.

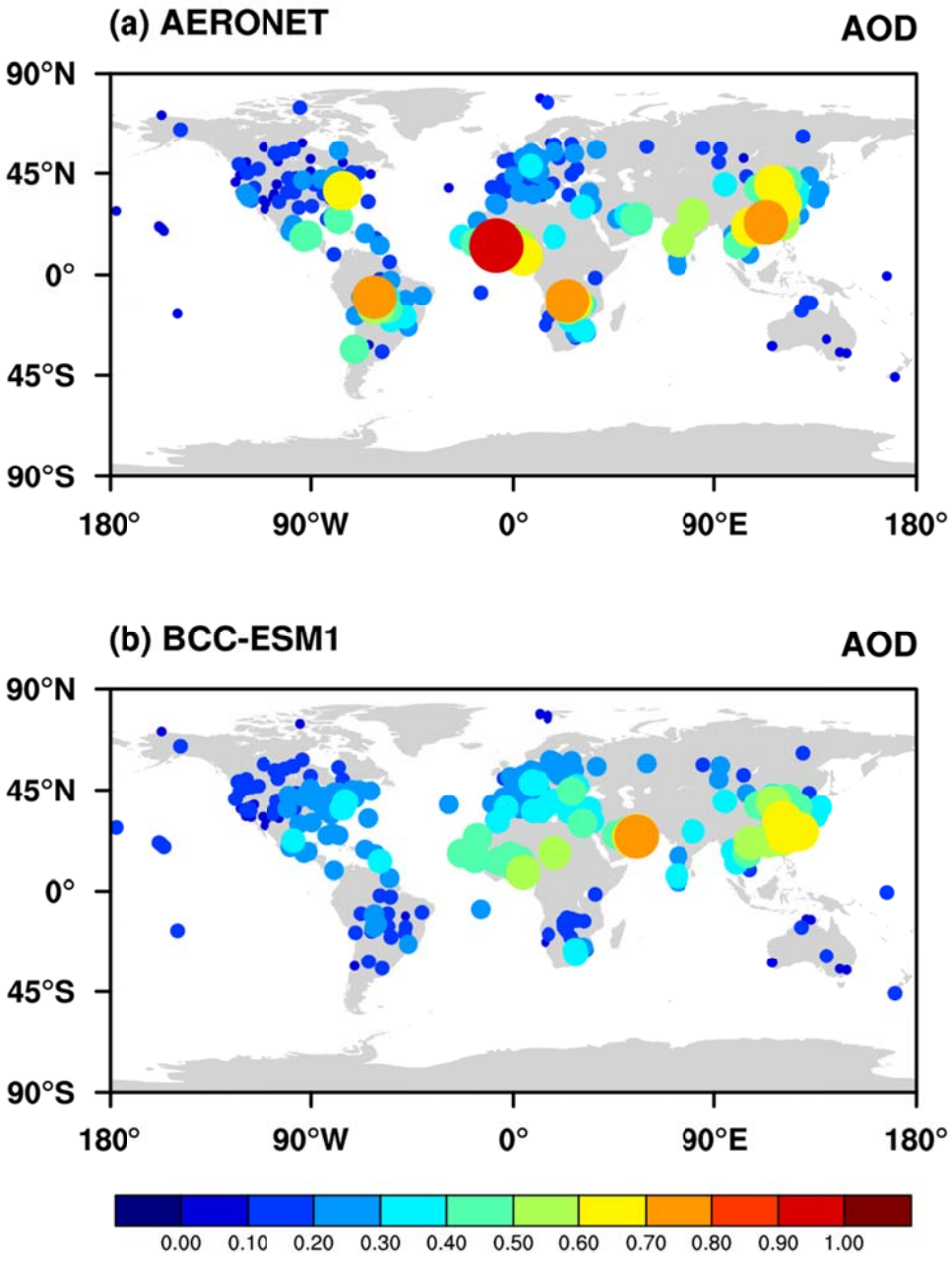

Figure 18. Observed versus simulated annual means of AOD at AERONET sites. Each data point represents the mean averaged for available monthly values of AOD. The dot sizes denote the magnitudes of AOD at sites. The spatial correlation is 0.56.

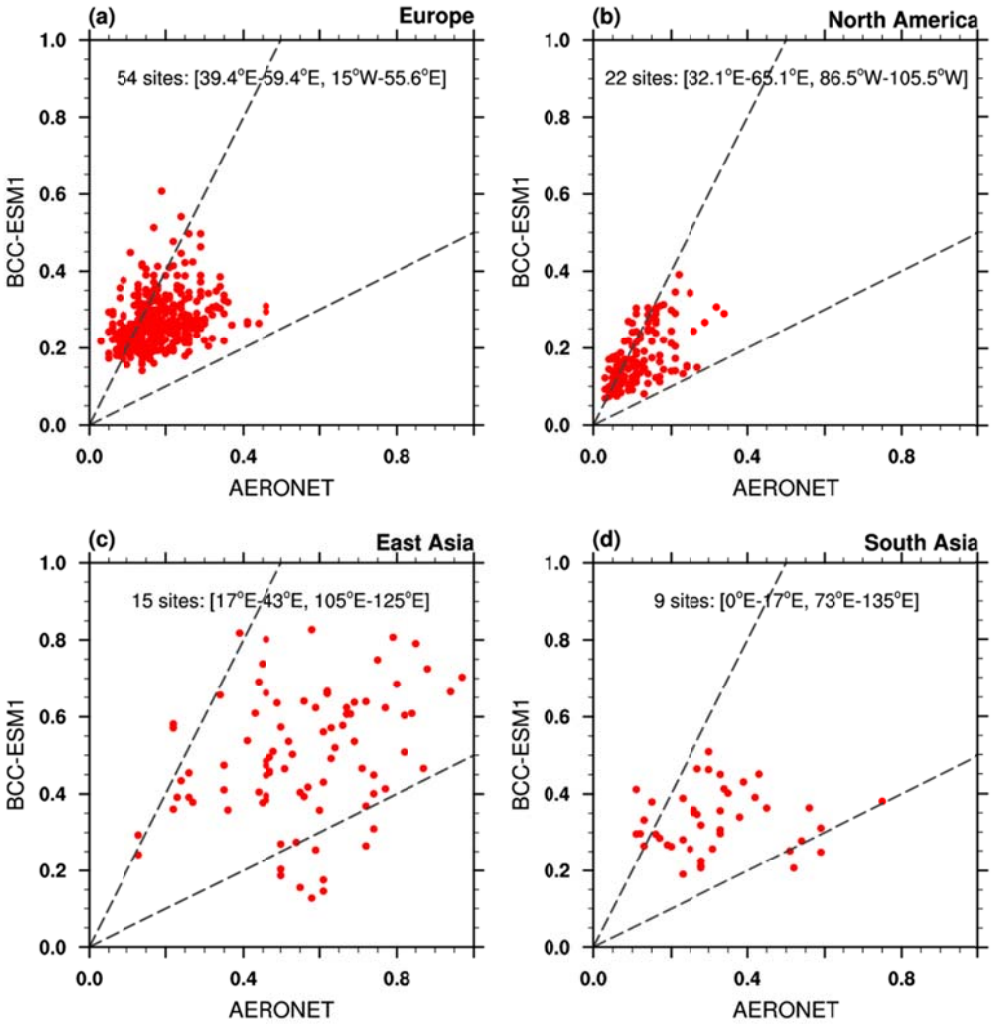

Figure 19. Scatter plots of observed versus simulated monthly mean AOD at AERONET sites in Europe, North America, East Asia, and South Asia over the period of 1998-2005.